# New insights into seismic absorption imaging

Panayiota Sketsiou[a,*], Ferdinando Napolitano[b], Aristides Zenonos[a], Luca De Siena[a,c]

[a] Department of Geology and Petroleum Geology, University of Aberdeen, Meston Building, King's College, Aberdeen AB24 3UE, United Kingdom
[b] Dipartimento di Fisica "E. R. Caianiello", Università degli Studi di Salerno, Via Giovanni Paolo II, Fisciano 84084, (SA), Italy
[c] Institute of Geosciences, Geophysics and Geodynamics, Johannes Gutenberg University, Mainz, Germany

ABSTRACT

In recent years, attenuation has been used as a marker for source and dynamic Earth processes due to its higher sensitivity to small variations of lithospheric properties compared to seismic velocity. From seismic hazard analysis to oil and gas exploration and rock physics, many fields need a better reconstruction of energy absorption, a constituent of seismic attenuation generally considered a reliable marker of fluid saturation in space. Here, we propose absorption tomography (AT), a technique grounded on the principles of scattering tomography and Multiple Lapse Time Window Analysis. We benchmark its efficiency to image absorption in space by comparing its results with those obtained using two of the most common mapping strategies, regionalization and kernel-based inversion for a diffusive regime. We applied these methodologies to three datasets, each characterized by a different tectonic setting and quality of the dataset: the Pollino fault area (Southern Italy), Mount St. Helens Volcano (USA) and Vrancea (Romania). AT overcomes the assignment of a single coda quality factor value between each source-receiver pair by modelling and inverting for the spatial distribution of energy as a function of different lapse times. It can then reconstruct node-dependent envelopes using analytic and computational sensitivity kernels and solve for coda attenuation with a grid-search approach. AT allows for a better reconstruction of the localized absorption anomalies than standard methodologies, even if the efficiency of the technique depends on the quality of the dataset, and identifies outliers in the data that could alter the final result and its interpretation. The implementation of analytical diffusive kernels in AT allows for a fast and highly-resolved imaging of well-sampled seismic faults structures. While slightly reducing resolution on faults and being computationally more expensive, implementing multiple-scattering lapse-time-dependent kernels still provides satisfactory results as well as a more physically-correct forward model.

## 1. Introduction

Seismic attenuation is one of the most important and least understood physical mechanisms affecting wave propagation in the Earth. Intrinsic and scattering attenuation, geometrical spreading, anisotropy, phase conversions and reflections all reduce coherent wave energies: despite, and often due to, these complexities, researchers have learned to use attenuation mechanisms to characterize structures and dynamics of the Earth from rock samples to the global scale (Carcolé and Sato, 2010; Eken, 2019; Li and Cormier, 2002; Przybilla et al., 2009; Romanowicz, 1995; Tisato et al., 2015; Wegler, 2003).

The success of attenuation as a marker for source and dynamic Earth processes is due to its higher sensitivity to small changes in the Earth matrix than, e.g., seismic velocities (Johnston and Toksöz, 1981). This sensitivity makes seismic attenuation a valuable estimator of geologic structures in soil engineering (Rodríguez-Pradilla, 2015; Xia, 2014) and

seismic hazard analysis (McNamara et al., 2014; Parolai, 2014), oil and gas exploration (Carcione, 2000) and rock physics (Rodríguez-Pradilla, 2015). The interest in seismic-wave attenuation as a tool to mark Earth heterogeneity and global-imaging attributes is steadily growing (Romanowicz, 1995). At sample scale, where both heterogeneity and saturation can be controlled, attenuation is a standard marker of fluid saturation and fluid-rock interaction (Picotti et al., 2010; Tisato et al., 2015), with successful applications to imaging and monitoring of resources (Carcione, 2000).

We refer to *attenuation* as the entire process of losing energy while the seismic wave propagates through the medium heterogeneities, i.e., the combination of scattering and seismic absorption, in addition to the smooth decrease of seismic energy due to geometrical spreading. *Absorption* is the irreversible mechanical energy loss through heat, caused by fluids and grain boundary friction (Carcione, 2000). *Scattering* is the mechanism which describes how small-scale

---

heterogeneities (or "scatterers", such as fractures or faults in the crust) spread energy in space (Sato et al., 2012). Total attenuation is described by the quality factor $Q$, that represents the relative loss of energy per seismic cycle. Moreover, $Q$ is a frequency-dependent quantity for frequencies higher than 1 Hz (Aki, 1980), defined as

$$Q^{-1} = Q_i^{-1} + Q_{sc}^{-1} \qquad (1)$$

where $Q_i^{-1}$ is the absorption (or intrinsic attenuation) inverse quality factor and $Q_{sc}^{-1}$ is the scattering inverse quality factor. $Q^{-1}$, $Q_i^{-1}$ and $Q_{sc}^{-1}$ are all dimensionless quantities.

In this paper, we will mainly focus on coda-wave intensities and intrinsic attenuation. Coda waves are the wave-trains following direct-wave phases at a given lapse-time from the origin time of the earthquake (Aki, 1980; Sato et al., 2012). Depending on lapse-time, scale, and frequency, coda waves are evidence of single-scattering (Aki and Chouet, 1975; Li and Cormier, 2002), multiple-scattering (Calvet and Margerin, 2013; Przybilla et al., 2009), or diffusion (Wegler, 2003). Once we define the scattering regime that best models coda waves, their decrease vs lapse time (measured by the coda quality factor, $Q_c$) can be used to map Earth structures from local to regional scale, from tectonic to volcanic settings (Calvet et al., 2013; De Siena et al., 2016; Mayor et al., 2016; Ogiso, 2018; Wang and Shearer, 2017).

Coda wave attenuation is an ideal tool to image strong lateral variations in lithospheric properties, and several techniques have been developed to assess these variations. The first step, common to all these techniques, consists of computing energy density envelopes of coda waves to obtain a coda quality factor, $Q_c$, value for each waveform. The energy within the coda window, $E(t,f)$, at fixed lapse-time $t$, in seconds from the origin time (see Havskov et al. (2016) for a review) and frequency $f$ is modelled using the following equation (Aki and Chouet, 1975):

$$E(t, f) = S(f) t^{-\alpha} \exp\left(-\frac{2\pi f t}{Q_c(f)}\right) \qquad (2)$$

where $S(f)$ is the frequency-dependent source term and $\alpha$ is a constant related to geometrical spreading, fixed a priori due to the fact that $\alpha$ and $Q_c$ co-vary in the equation. Its value depends on the physical model used to describe coda waves: in a *single-scattering* interpretation $\alpha$ is set equal to 2 and $Q_c$ is tied to both scattering and absorption as $Q_c^{-1} = Q_{sc}^{-1} + Q_i^{-1}$; in a *multiple-scattering* interpretation $\alpha = 3/2$ and $Q_c \approx Q_i$, if, after a few mean free times (mean time between two scattering events), the diffusion regime is reached (Calvet et al., 2013). Multiple scattering is the best regime to model high-frequency coda waves just a few seconds after the direct S-wave (e.g., Przybilla et al., 2009). It can lead more or less rapidly to the onset of equipartition (Hennino et al., 2001), a necessary condition for the onset of diffusion. In the Pyrenees, Souriau et al. (2011) demonstrated that the equipartition regime could be reached only a few seconds after the S-waves arrival. In volcanic media, equipartition and the onset of diffusion are observed immediately after the S-wave arrival (Wegler, 2003), after a few seconds from it (De Siena et al., 2013), or tens of seconds after the S-wave arrival (De Siena et al., 2016) depending on scale, topography, and boundary conditions.

Different methodologies have been developed to image attenuation in the lithosphere, in a multiple-scattering regime: with extensive datasets, researchers have been able to separate the contribution of seismic scattering and absorption, then regionalizing their spatial variations and enhancing the interpretation of the main geological features imaged. Carcolé and Sato (2010) obtained separate maps of scattering and intrinsic attenuation in Japan using the Multiple Lapse Time Window Analysis (MLTWA, Fehler et al., 1992). Another methodology for separating intrinsic and scattering attenuation of seismic waves is by envelope inversion, as demonstrated by Eulenfeld and Wegler (2016) who also developed the *Qopen* software by implementing this method. The same authors used *Qopen* to map the intrinsic and scattering

attenuation of the crust in the contiguous USA, using data from the USArray (Eulenfeld and Wegler, 2017). Similarly to Eulenfeld and Wegler (2016), Ogiso (2018) used an envelope fitting method to estimate the site, source, intrinsic and scattering attenuation factors in southwestern Japan, assuming isotropic scattering. The 3D mapping of these parameters was done using sensitivity kernels calculated by a Monte Carlo simulation, modelling both the envelopes and their derivative (Takeuchi, 2016). The depth variations in scattering parameters between crust and mantle are often modelled by a two-layer approximation of the technique (Del Pezzo and Bianco, 2010). Radiative-transfer-based simulation of one and two-layer structures lead to imaging of scattering and absorption in the lithosphere in volcanoes (De Siena et al., 2013; Prudencio et al., 2013) and at regional scale (Przybilla et al., 2009; Wang and Shearer, 2017). Scattering attenuation can be measured with a data-driven approach, using peak-delay times as a marker of forward scattering attenuation (Takahashi et al., 2007) while $Q_c$ at late lapse times, where equipartition takes place (Calvet and Margerin, 2013; Hennino et al., 2001) can be used as a marker of absorption. With these measurements, Calvet et al. (2013) and De Siena et al. (2016) mapped scattering and absorption in the Pyrenees mountain range and at Mount St. Helens volcano (USA), respectively.

While $Q_c$ can be mapped using a regionalization approach, recent advancements propose the use of space weighting functions and sensitivity kernels (Del Pezzo et al., 2016; Mayor et al., 2014; Obermann et al., 2013) for the imaging of the spatial variations of $Q_c$ at crustal and local volcanic scale (Borleanu et al., 2017; De Siena et al., 2017; Mayor et al., 2016). By exploiting the rapid onset of diffusion in volcanoes (De Siena et al., 2013; Wegler, 2003), De Siena et al. (2017) developed a procedure for the inversion of $Q_c$, where the main assumption is that total coda attenuation is caused by a single diffusive layer (i.e., absence of leakage and crustal pinching). Recent research shows that this assumption is simplistic at local-to-regional scale (Margerin, 2017; Sanborn and Cormier, 2018; Wang and Shearer, 2017).

In this study, we propose an alternative methodology for kernel-based coda-attenuation tomography. The method targets multiple-scattering crustal media at late lapse times, testing equipartition, then mapping coda-attenuation with diffusive kernels and interpreting $Q_c$ variations in terms of absorption (thus the name *Absorption Tomography — AT*). We employ both linear and non-linear measurements of source-receiver $Q_c$ and discuss their effect on tomographic imaging. The AT is a diffusive equivalent of the single scattering tomography proposed by Nishigami (1991). His method extracted small windows across the envelope starting from just after the direct-wave arrival, back-projected them in space, then interpreted their intensity with a single-scattering model and regionalized the variations. The results highlight zones of high scattering at surface and across faults; when applied to volcanoes, Nishigami's technique is able to define caldera rim structures (Tramelli et al., 2006) as well as deep plumbing systems and magma accumulation in the crust (De Siena et al., 2014). With a procedure similar to MLTWA (Carcolé and Sato, 2010; Del Pezzo and Bianco, 2010; Fehler et al., 1992) the AT divides the energy envelopes of late coda waves, where equipartition takes place, into smaller windows, and maps each window separately in space using diffusive sensitivity kernels (Del Pezzo et al., 2016). Differently from most applications of coda-attenuation imaging, which use a regionalization (averaging) approach, the AT uses the inversion procedure laid out by De Siena et al. (2017), assuming energy-propagation in a single layer and absorbing boundary conditions. The method has been applied to three datasets at different scales to test it depending on the quality of datasets and differences in geological settings: Pollino area (fault zone — Southern Italy), Mount St. Helens (volcano — USA) and Vrancea (regional — Romania). The results were compared with those obtained with a standard $Q_c$ regionalization approach and kernel-based inversion in order to estimate the improvement in geological features reconstruction. The AT procedure is independent of the sensitivity kernel chosen: both a lapse-time-independent analytic kernel (Del Pezzo et al., 2016) and a multi-

scattering lapse-time-dependent kernel (Del Pezzo et al., 2018; Paasschens, 1997; Pacheco and Snieder, 2005) were thus used, the second being more computationally expensive but a better representative of the scattering process.

## 2. Coda attenuation imaging

In this work, we apply the standard coda attenuation imaging using a regionalization approach (hereafter called M0 — e.g., Calvet et al., 2013 , described in Section 2.1) and an inversion scheme based on diffusive sensitivity kernels (M1 — De Siena et al., 2017 ; Section 2.2) to image seismic absorption in the 2D space. These two methodologies are used as benchmarks for the new technique, AT, which uses concepts developed in scattering tomography and MLTWA.

### 2.1. Coda attenuation imaging using a standard regionalization approach (M0)

In order to map $Q_c^{-1}$ values in space, it is essential to know what is the sensitivity of coda waves to space. In the diffusive propagation model, the coda waveforms have higher sensitivity to slowness or scattering perturbations around the source and the receiver (e.g., Mayor et al., 2014). The 2D mapping of the measured $Q_c$ values is generally obtained by regularizing. A simple regionalization approach, adopted e.g. by Calvet et al. (2013) and De Siena et al. (2016) consists of assigning $Q_c$ values to ray-paths between each source and receiver. To account for the fact that the sensitivity of coda waves is higher close to the source and the receiver, Calvet et al. (2013) recommended that $Q_c$ measurements for small epicentral distances should be selected. Nevertheless, this strongly depends on the size of the area being mapped. In their study of the Pyrenees, they used epicentral distances up to 90 km. At Mount St. Helens (MSH) volcano, De Siena et al. (2016) considered all the epicentral distances since the size of their study area was significantly smaller. An alternative approach is to assume $Q_c$ can be mapped as station dependent only (e.g., Carcolé and Sato, 2010 ; Wang and Shearer, 2019). This assumption is especially valid when heterogeneity increases and thin shallow features may dominate mapping at specific frequencies (De Siena et al., 2016).

The parametrization of these studies depends on both the number and the distribution of sources and receivers, and it is imposed *a priori* on the area. When a sufficient number of rays, each characterized by a $Q_c$ value, propagates inside a block, the mean $Q_c$ value from all the rays is allocated to it. Only blocks crossed by at least two ray-paths are taken into account. In order to smooth the spatial variations and create the final map, an average of the mean $Q_c$ value over the nearest blocks is taken (usually the nine nearest blocks are widely chosen). The $Q_c$ maps are obtained in different frequency bands. Generally, it is known that waves of lower frequencies can detect bigger structures, while higher frequencies highlight smaller structures. However, whether these are shallow or deep depends on the geology of the area; as this is a 2D analysis, the maps are an average of all depths. The methodology described in this section will be hereafter called M0.

### 2.2. Coda attenuation imaging using sensitivity kernels (M1)

#### 2.2.1. Approximate analytical sensitivity kernels for coda attenuation imaging

For a *single scattering* approximation, the spatial sensitivity of coda waves is represented by an ellipsoid (Aki and Chouet, 1975). As the lapse time and frequency increase, the waves enter into multiple scattering and diffusion regimes, where the spatial sensitivity becomes more complex. In a *multiple scattering* regime, coda waveforms are more sensitive to perturbations around the source and the receiver than to the remaining medium (Del Pezzo et al., 2016; Mayor et al., 2014; Obermann et al., 2013). In the following, we discriminate between space-weighting functions and sensitivity kernels. *Space-weighting* is the

chosen expression when the analytic or numeric functions, developed using different physical models, are used to weight-average coda measurements across the nodes of a grid. We name the same functions *sensitivity kernels* when they are used to perform a tomographic inversion in space.

Prudencio et al. (2013) developed and applied Gaussian space-weighting functions mimicking the increased coda sensitivity to source and receiver positions. Obermann et al. (2013) studied the depth sensitivity of coda waves to velocity perturbations and developed corresponding sensitivity kernels for multiple scattering and diffusion using the radiative transfer theory. They concluded that the depth sensitivity of coda waves is related to both the body and surface wave sensitivity. Mayor et al. (2014) developed sensitivity kernels in 2D isotropically-scattering media for energy absorption and scattering. Their diffusive kernels depend on the coda lapse time and the type of perturbation and were applied as space-weighting functions for absorption imaging (Mayor et al., 2016). Del Pezzo et al. (2016) and Del Pezzo et al. (2018) developed similar 2D and 3D diffusive space-weighting functions for coda wave back-projection mapping. They solved the Energy Transport Equation using Monte Carlo methods, focusing on high-heterogeneity volcanic areas. We remark that the diffusive kernels (or space weighting functions) developed by different authors are all very similar, with peaks at source and receivers and increased lateral sensitivity with respect to a line approximation (Fig. 1).

Del Pezzo et al. (2016) discuss in detail the limit of the line (or strip) and Gaussian space-weighting functions approaches when compared to the use of proper space-weighting functions developed with radiative transfer theory. They derive an approximate kernel which accounts for 95% of the spatial variations of coda energy in the diffusive regime. These approximate diffusive kernels do not depend on lapse time and have been tested in volcanic environments and where the diffusion approximation is valid. Their analytic form, i.e., the forward model of the spatial inversion, is the kernel associated to the $i^{th}$ event and the $j^{th}$ station:

$$F1_{i,j}[x, y, x_r, y_r, x_s, y_s, \delta_x, \delta_y] = \frac{1}{4\pi\delta_x D^2 \delta_y}\exp\left[-\frac{\left(x - \frac{x_r + x_s}{2}\right)^2}{2(\delta_x D)^2} + \frac{\left(y - \frac{y_r + y_s}{2}\right)^2}{0.5(\delta_y D)^2}\right]$$
$$+ \frac{1}{2\pi\delta_x D^2 \delta_y}\exp\left[-\frac{(x - x_s)^2}{2(\delta_x D)^2} + \frac{(y - y_s)^2}{2(\delta_y D)^2}\right]$$
$$+ \frac{1}{2\pi\delta_x D^2 \delta_y}\exp\left[-\frac{(x - x_r)^2}{2(\delta_x D)^2} + \frac{(y - y_r)^2}{2(\delta_y D)^2}\right]$$

(3)

where $x_s, y_s$ are the source coordinates, $x_r, y_r$ are the receiver coordinates, $\delta_x, \delta_y$ is the spatial aperture of the weighting function and $D$ is the horizontal source-receiver distance (Del Pezzo et al., 2016).

#### 2.2.2. Lapse-time-dependent sensitivity kernels for coda attenuation imaging

Kernel $F1$ is an analytic lapse-time-independent approximation only valid in the diffusive regime; while it speeds up computation and is useful to define the preliminary tomographic problem, a lapse-time-dependent ($t$) multiple scattering kernel is the best choice to model the effective sensitivity of the process. We thus use a second kernel ($F2_{i,j}$) as forward model in the tomographic approach: this computational kernel adopts the Paasschens (Paasschens, 1997) approximation of the Energy Transport Equation solution in three dimensions to describe the seismogram energy envelope:

$$E_{i,j}^{3D}[r_{ij}, t] \approx \frac{W\exp[-Le^{-1}vt]}{4\pi r_{ij}^2 v}\delta\left[t - \frac{r_{ij}}{v}\right] + WH\left[t - \frac{r_{ij}}{v}\right]\cdot$$
$$\frac{\left(1 - \frac{r_{ij}^2}{v^2 t^2}\right)^{1/8}}{\left(\frac{4\pi vt}{3B_0 Le^{-1}}\right)^{3/2}}\cdot\exp[-Le^{-1}vt]G\left[vtB_0 Le^{-1}\left(1 - \frac{r_{ij}^2}{v^2 t^2}\right)^{3/4}\right]$$

(4)

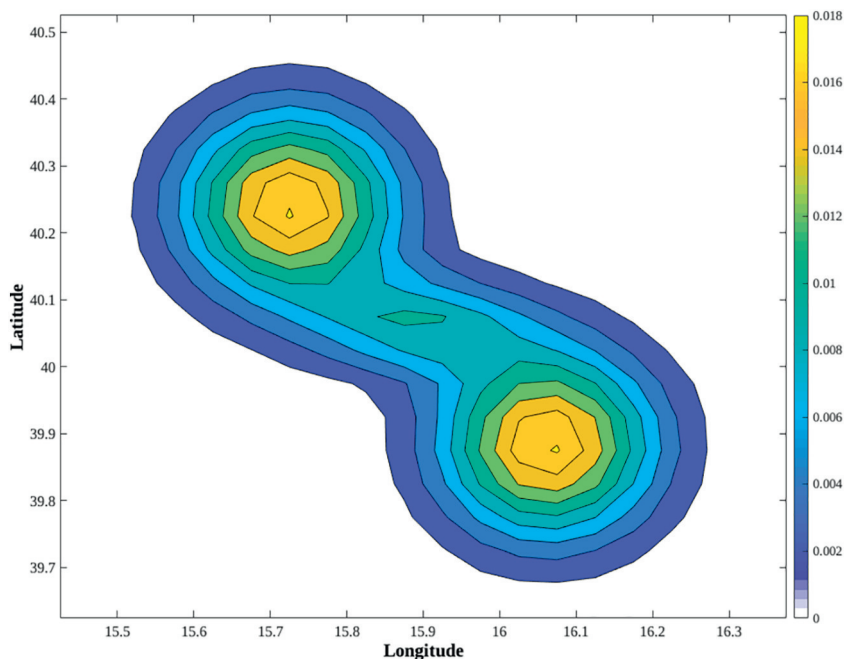where $G[s] = e^s\sqrt{1 + 2.026/s}$ and $\delta$ and $H$ are the Dirac delta and the

**Fig. 1.** Example of a 2D sensitivity kernel normalized across space obtained using the analytical function by Del Pezzo et al. (2016) for a specific source-receiver pair (*F1*).
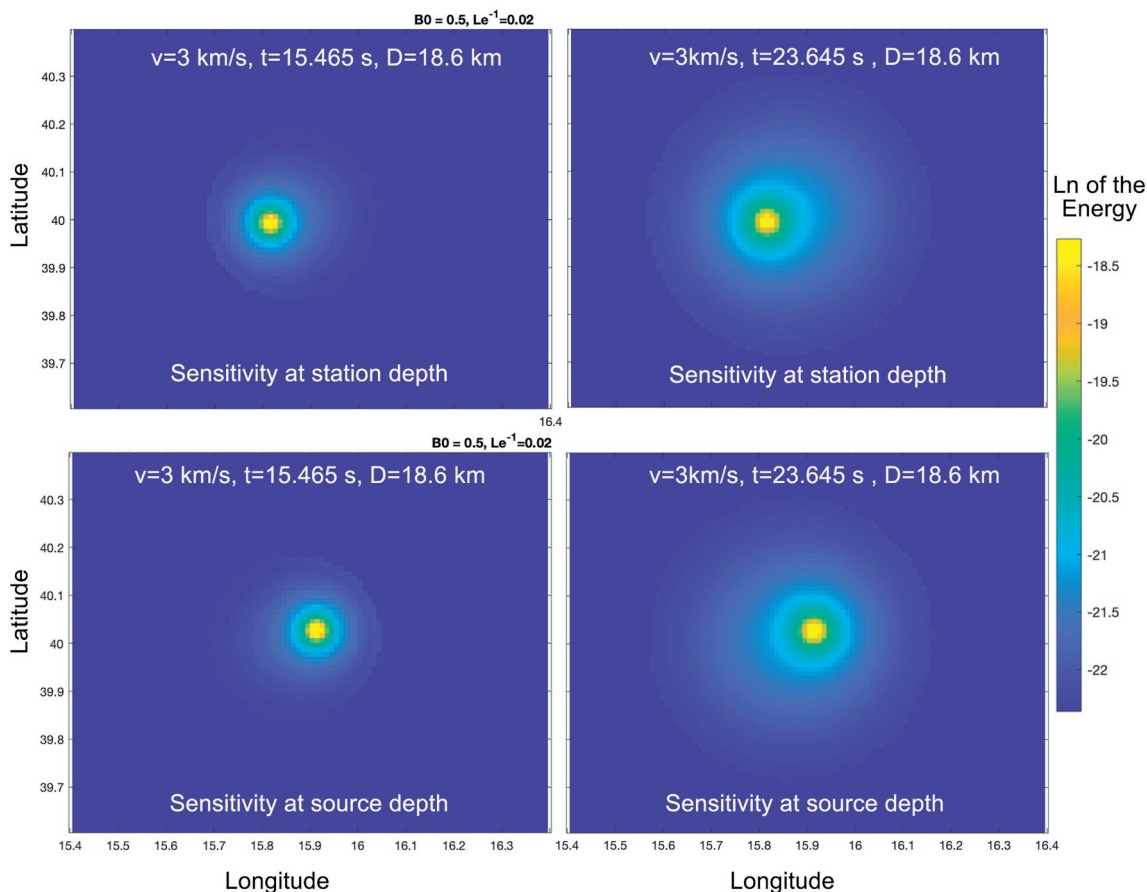


**Fig. 2.** Two example slices at source and receiver depth showing the 3D sensitivity kernels (*F2*) obtained at different lapse times using the computational codes from Del Pezzo et al. (2018) for a specific source-receiver pair at distance *D*.

Heaviside step functions, respectively. Here, $W$ is the source energy, $v$ is the seismic velocity, $r_{ij}$ is the 3D source-station distance and $t$ is the lapse time. Fitting Eq. (4) to the experimental energy envelopes, the

single-path separate estimate of the scattering albedo ($B_0$) and extinction length $Le^{-1}$ is possible (see Ogiso (2018) for a recent application). Here, we focus on the corresponding spatial sensitivity using the
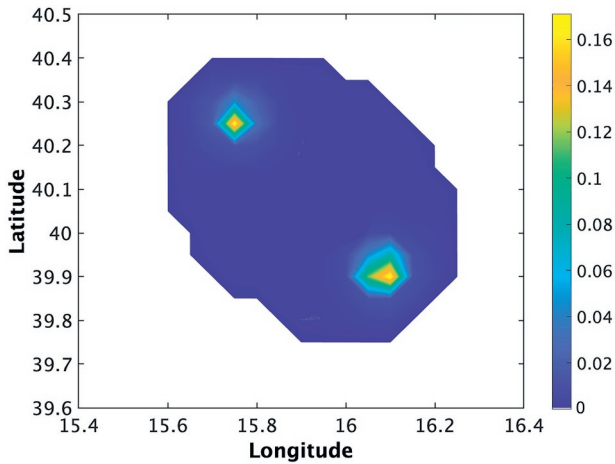
**Fig. 3.** Example of a 2D sensitivity kernel normalized across space obtained by compressing to 2D the 3D sensitivity kernels (*F*2).

hypothesis of Pacheco and Snieder (2005), setting $v = 3.5\,\text{km/s}$, $B_0 = 0.5$ and $Le^{-1} \cong \frac{2\pi f}{v}Q_{coda}^{-1}$ at average values for the crust:

$$F2_{i,j}^{3D}[\varrho, t, B_0, Le^{-1}, v]$$
$$= \int_0^T E^{3D}[r_{s\varrho}, \tau, B_0, Le^{-1}, v]E^{3D}[r_{\varrho r}, T - \tau, B_0, Le^{-1}, v]d\tau \tag{5}$$

where $\varrho$ is the space point with coordinates $\{i,j,z\}$, $r_{\varrho r}$ is the point-to-source distance and $r_{\varrho r}$ is the point-to-receiver distance. The kernels have been numerically computed using the codes in Del Pezzo et al. (2018): Fig. 2 shows two horizontal slices into the 3D model at source and receiver depths and for different lapse times for a source-station pair at $D018\,\text{km}$.

### 2.2.3. Definition of an inversion for the spatial sensitivity of Qc: use of different kernels

Even if they are developed to map energy distribution, the sensitivity kernels in Eqs. (3) and (5) have been used to invert for the spatial distribution of $Q_c^{-1}$ at late lapse times and thus obtain a map of the absorption structure of the study area. To date, the only studies to apply an inversion procedure (hence, one that can be tested with synthetics) to coda sensitivity kernels are De Siena et al. (2017) for the 2D and Akande et al. (2019) for the 3D case. The study area is Campi Flegrei caldera, southern Italy. In the 2D inversion (De Siena et al., 2017), the elements of the data vector are the source-receiver measurements of $Q_c$. After imposing a grid on the study area, Eq. (3) is computed and used as a sensitivity kernel for the inversion of $Q_c$. The inversion matrix (**G**) has rows corresponding to the sensitivity kernels normalized to their maximum value. The normalization implies that the total coda energy can be modelled by its spatial interaction with the grid only, i.e., no energy leaks out of the gridded medium (Margerin, 2017; Sanborn et al., 2017).

Any of the above-mentioned diffusive sensitivity kernels can be implemented similarly: the main advantage of the one defined in Eq. (3) (*F*1) is that it allows to greatly speed up the computation time for tomographic purposes, obtaining a preliminary map of energy distribution and corresponding coda attenuation. Nevertheless, the kernel in Eq. (5) (*F*2) better describes the physics of the process, at least given adequate input parameters. In order to compare the results obtained with different kernels, we will compress to 2D the 3D *F*2 kernels by averaging across depth: the procedure is the same described by De Siena et al. (2016), with the difference that these authors were using simple ray-dependent sensitivity. Fig. 3 is obtained for the same source-station pair of Fig. 1, a result similar to those obtained by other authors (e.g., Margerin et al., 2015). The comparison of *F*1 and *F*2 shows that
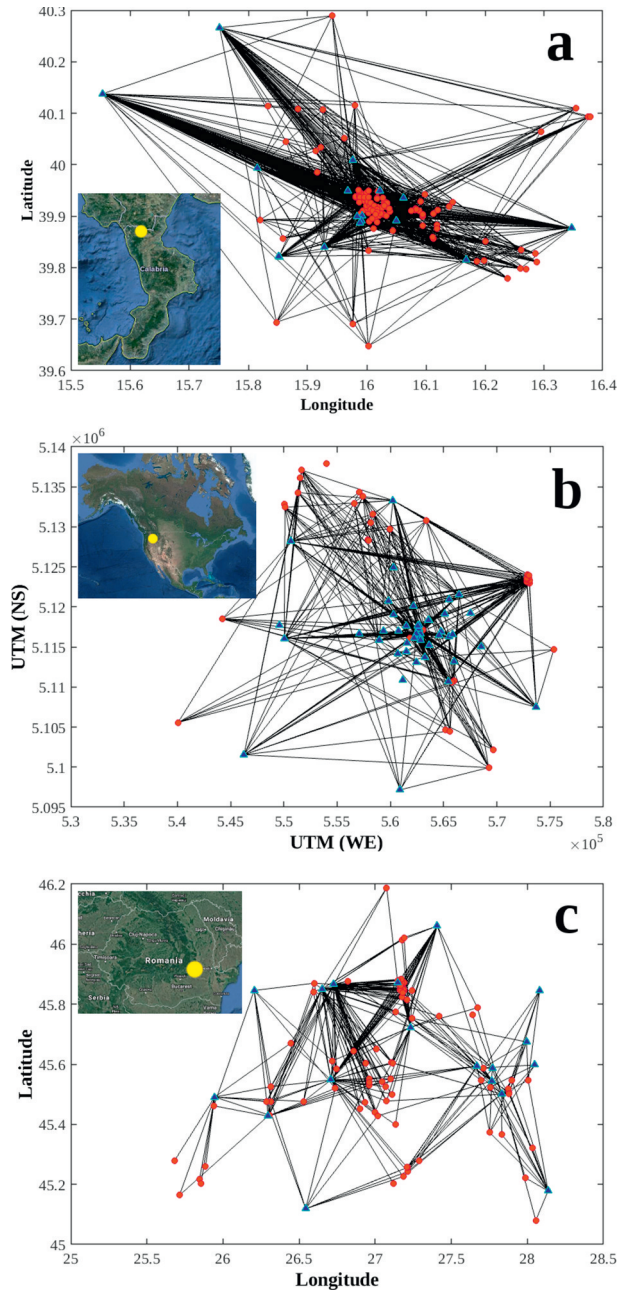


**Fig. 4.** Ray coverage in: (a) Pollino area (Southern Italy); (b) Mount St. Helens (USA); (c) Vrancea (Romania). Red circles represent the seismic sources, blue triangles represent the seismic stations with at least one recording. The central panel shows UTM coordinates instead of Latitude-Longitude due to the information stored in the SAC header. (For interpretation of the references to color in this figure legend, the reader is referred to the web version of this article.)

the analytic approximation *F*1 apparently overestimates the sensitivity of the coda to the source-station segment at the expense of the illumination provided by the single scattering ellipsoid.

The resulting linear inverse problem can be solved using a zeroth-order Tikhonov regularization. The solution is a matrix of a $Q_c^{-1}$ value for each block of the grid. Differently from the regionalization approach, setting an inversion problem allows to test resolution and stability of the solution (Rawlinson and Spakman, 2016). An *L*-curve is created to give an estimate for the regularization parameter but usually several regularization parameters are tested. To assess the goodness of the result, researchers can also perform synthetic tests. The method

**Table 1**
Summary of the parameters used to compute $Q_c^{-1}$ values for the three datasets. The second column shows the central frequency range used for filtering, the third column shows the moving window parameter used for envelope smoothing, the fourth and fifth columns show the starting lapse time in seconds starting from the origin time, $t_c$, and the length of coda window $L_w$ in seconds, respectively.

| Dataset | Frequency bands (Hz) | nf | $t_c$(s) | $L_w$(s) |
|---------|----------------------|-----|----------|----------|
| Pollino | 2–4, 4–8, 6–12, 8–16, 10–20 | 4 | 15 | 10 |
| MSH | 2–4, 4–8, 6–12, 8–16, 10–20, 12–24 | 8 | 20 | 15 |
| Vrancea | 2–4, 4–8, 6–12, 8–16, 10–20 | 8 | 25 | 15 |

described in this section will be hereafter called M1.

## 3. Data processing and methods

### 3.1. Datasets

The selection of a suitable dataset, in terms of the amount of data, ray coverage, quality of the waveforms and accuracy of their pre-processing (e.g. re-location of the events extracted from a catalogue, precise P- and S-waves pickings, complete header setup), is crucial in order to obtain reliable results from imaging studies. Here, we aim to apply Absorption Tomography (AT) to three different datasets of decreasing coverage and quality: Pollino area (Southern Italy), Mount St. Helens (USA) and Vrancea (Romania). The differences among the three datasets heavily affect our confidence in the results, precluding in some cases the possibility to link the main patterns coming out from the attenuation images with the local geological structures. The comparison allows to benchmark the minimum quality a dataset must have to apply any of the techniques discussed, and particularly AT.

### 3.1.1. Pollino area dataset

The west section of the Pollino Range, located at the border between Calabria and Basilicata regions in Southern Italy, was affected by a swarm-like sequence of more than 10,000 low-to-moderate earthquakes

between 2010 and 2014 (Margheriti et al., 2013). Part of these data, already used in combination with geological and remote-sensing data to map seismically-active faults (Brozzetti et al., 2017) and to evaluate local site effects (Napolitano et al., 2018), and earthquakes of the surrounding area [lon: 15.4 –16.4(111 km); lat: 39.6 –40.4(70 km)] were selected to create a dataset composed of 117 local earthquakes, for a total amount of 911 waveforms recorded by 21 seismic stations from three different networks operated by *Instituto Nazionale di Geofisica e Vulcanologia (INGV)*, *GFZ* and *Università della Calabria*. The events were characterized by local magnitude between 1.8 and 4.3, depth between 1 and 52 m and epicentral distance between 1 and 72 km. The earthquakes, extracted from the ISC catalogue, have been firstly re-located and subsequently, the P-wave onsets were picked for the whole dataset, which also comprises 357 waveforms with clear picking of both P and S waves. The Pollino ray coverage is shown in Fig. 4a. The dataset is ideal to map the several and connected fault structures located in the area.

### 3.1.2. Mount St. Helens dataset

Mount St. Helens (hereafter MSH) is an active stratovolcano of the Cascadian arc located in Skamania County, Washington, in the Pacific Northwest region of the United States. After 18 years from the last eruption (on May 18, 1980), a new phase of eruption of MSH began in 2004. In the four years before the 2004 eruption the number of earthquakes in the area and their magnitude were low. We collected and used 64 events which occurred between 2000 and 2003, for a total amount of 451 waveforms recorded by the 13 stations of the Pacific Northwest Seismic Network (De Siena et al., 2016). These data are characterized by local magnitudes between 1.5 and 2.6, hypocentral distances between 5 and 60 km and depth between 1 and 20 km. The ray distribution (Fig. 4b) is not ideal, due to the number of earthquakes clustered just under the crater of the volcano being much higher than in the surrounding area, but still suitable for this analysis. The size of the study area is smaller than the Pollino one (40 km × 48 km), but the geological setting is significantly different. This is a typical dataset that can be used to image and monitor a volcano.
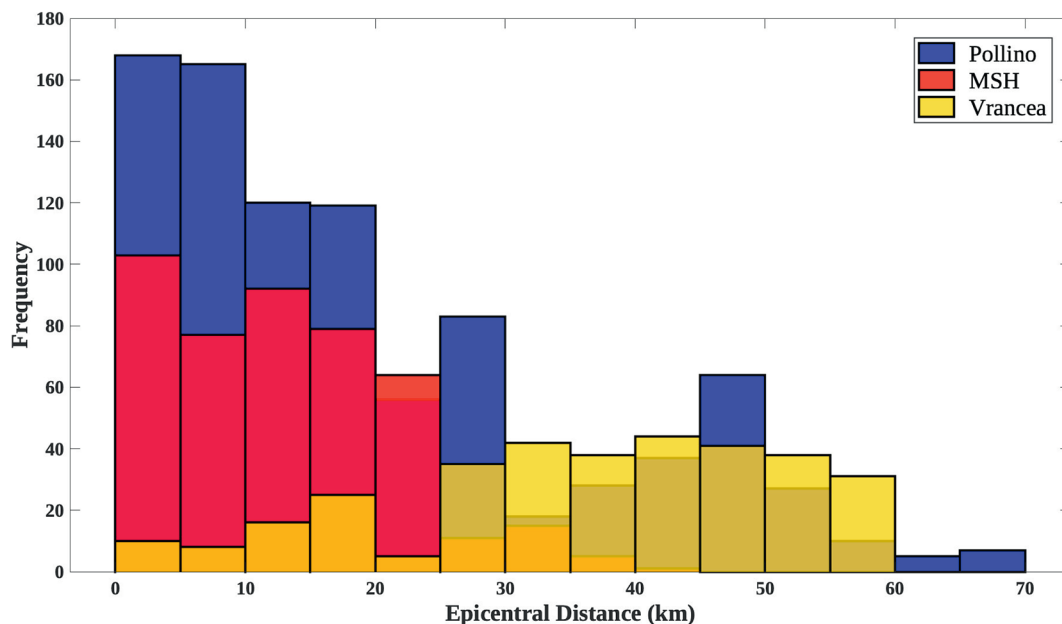


**Fig. 5.** Histograms representing the epicentral distances for the waveforms of the three analyzed datasets: blue colour for Pollino, red for Mount St. Helens (MSH) and yellow for Vrancea. MSH dataset is mainly composed by earthquakes located at epicentral distances above 30 km, while the Vrancea dataset is composed by earthquakes below this limit. The epicentral distances of the waveforms in the Pollino dataset span the 0–70 km range, with a higher percentage of local earthquakes extracted from the 2010–2014 seismic sequence. (For interpretation of the references to color in this figure legend, the reader is referred to the web version of this article.)

## Waveforms
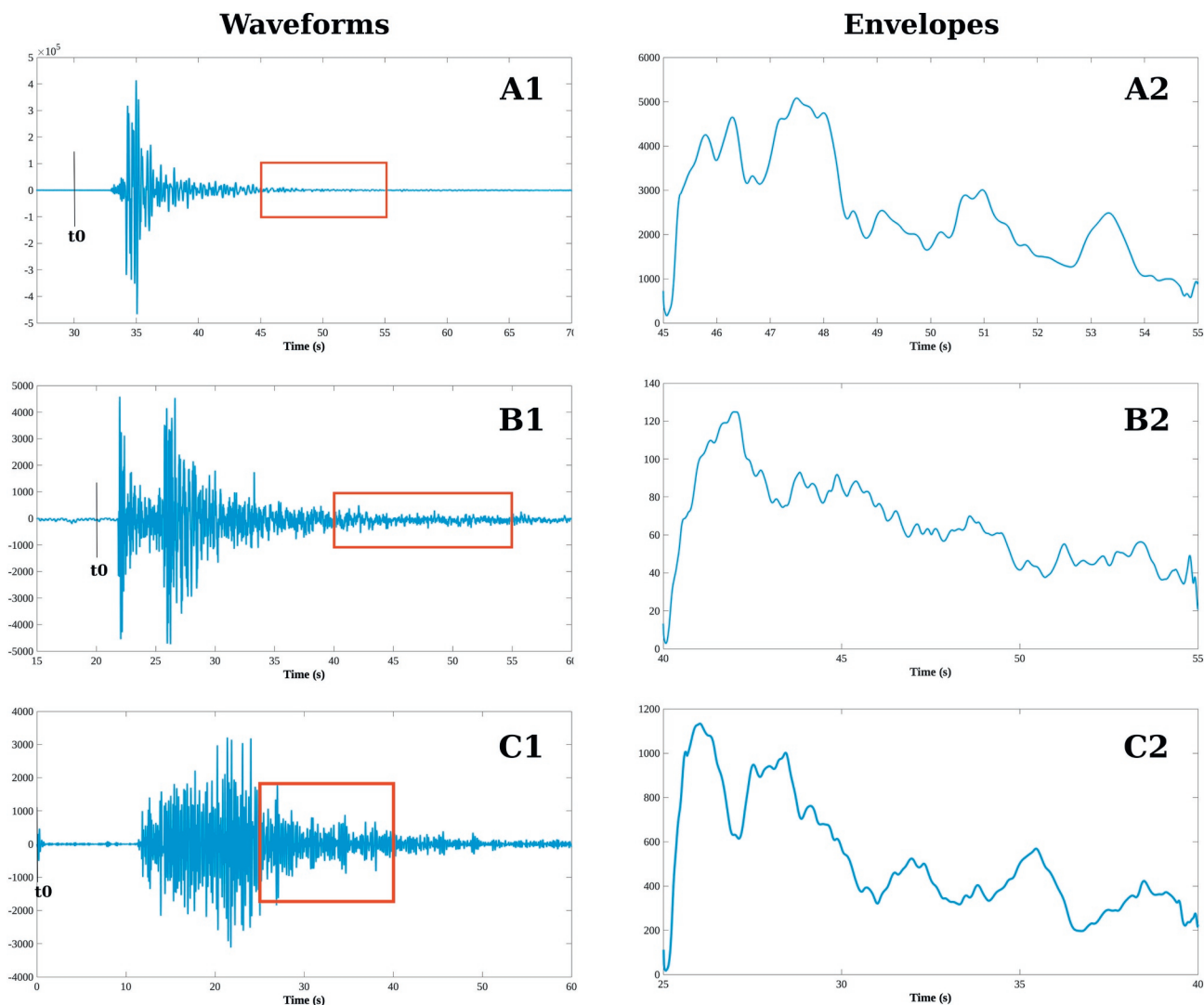
## Envelopes



**Fig. 6.** Example of a filtered waveform (6 Hz) for the Pollino area (A1), MSH volcano (B1) and Vrancea (C1). The selected coda window for each dataset is represented by a red box. The associated envelope computed in each coda window is shown on the right panels A2, B2 and C2 for Pollino, MSH and Vrancea respectively. The origin time of each earthquake, $t_0$, is marked. (For interpretation of the references to color in this figure legend, the reader is referred to the web version of this article.)

### 3.1.3. Vrancea dataset

The Vrancea region, located at the southeastern edge of the Carpathian Mountains arc bend in Romania, is one of the most seismically-active areas in Europe, characterized by crustal events of magnitude up to $M_W 6$, spread on a large area, and by strongly clustered intermediate-to-deep events characterized by magnitude up to $M_W 7.9$ (Borleanu et al., 2017).

The size of the study area is 330 km × 176 km, significantly bigger than Pollino and MSH. Despite the seismicity of the area, our dataset is poor and the ray coverage turns out to be insufficient to produce robust and reliable results. Indeed, the dataset consists of 80 local-to-regional earthquakes, for a total amount of 333 waveforms recorded between 2014 and 2017 by 18 seismic stations of the *Romanian Seismic Network (RSN)* operated by the *National Institute for Earth Physics (NIEP)*. The number of waveforms did not allow us to relocate the earthquakes. The only pre-processing we could perform on these waveforms consisted of the re-picking of P-wave onsets and the discarding of noisy traces. The resulting dataset comprises of events characterized by epicentral distances between 3 and 60 km, depth between 3 and 55 km and local magnitude ranging between 2.8 and 5.0. Fig. 4c shows the ray coverage for the Vrancea area.

### 3.2. Testing the onset of diffusion at different lapse times

As it has been explained in Section 1, the coda quality factor $Q_c$ at late lapse times is a measure of absorption when the multiple scattering approximation approaches the diffusion regime. A necessary (but not sufficient) condition to assess whether the coda window is in the diffusion regime is to test the equipartition of energy between the horizontal and vertical components, when all of them are available. While in the Pollino area all the components are accessible, this is not the case for MSH and Vrancea datasets. For the Pollino area, a coda window starting 15 s after the origin time is in the equipartition regime, as shown in Fig. S1 in Supplementary materials, using an earthquake of short (4 km) and one of long (44 km) epicentral distance. Energy equipartition for MSH was tested using a 2005 earthquake (epicentral distance of 10 km) and the results are shown in Fig. S2. Due to the lack of all the components, it is not possible to assess energy equipartition for Vrancea.The chosen procedure to select a preliminary coda window for Vrancea was thus to evaluate the distribution of earthquakes and stations with respect to the size of the area, using the criteria proposed by the extensive review of Havskov et al. (2016). Table 1 summarizes the starting lapse time and the length of the selected coda window for each of the three datasets.
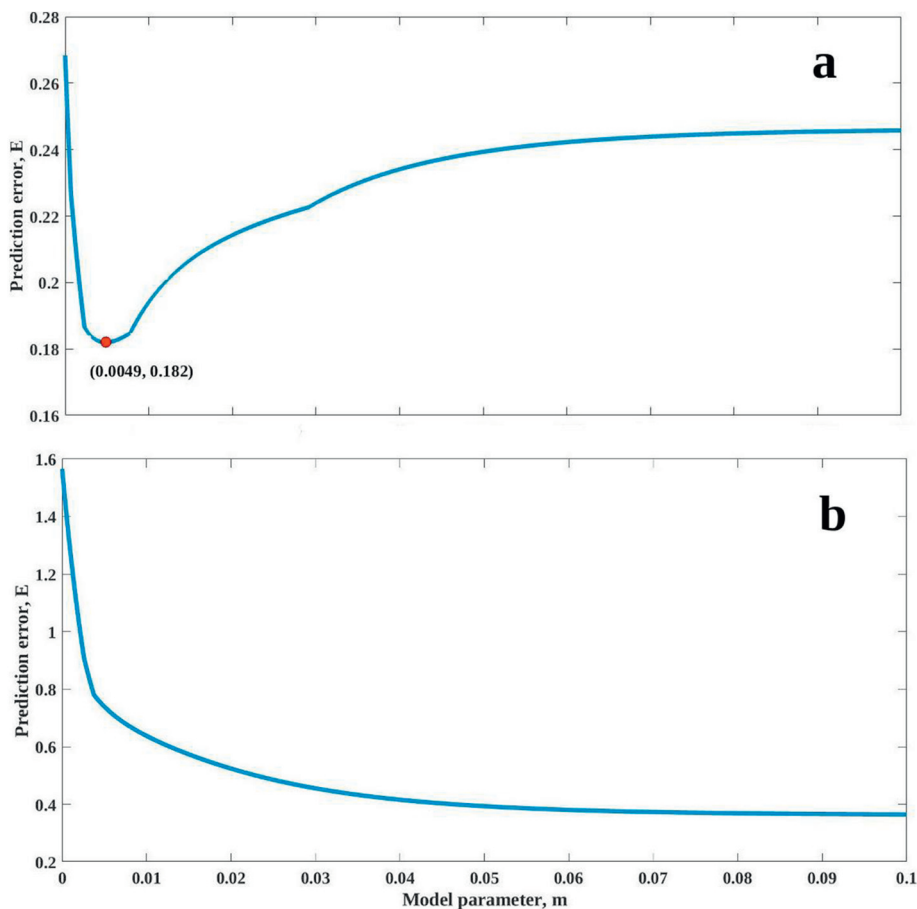
**Fig. 7.** Prediction error $E$ vs. model parameter, in this case $Q_c^{-1}$, for two different waveforms. Panel (a) shows the minimum (red point) of the misfit function computed using the grid search algorithm, whose x-coordinate represents the $Q_c^{-1}$ value ($Q_c^{-1} = 0.0049$) that better minimizes the difference between the observed and the predicted energy obtained by the envelope of the coda window. Panel (b) shows an example of a failure of the grid search algorithm, where a minimum is still found but it is not a single minimum. The best $Q_c^{-1}$ value is given by the first or last value of the model parameter range (in this specific case is the last value, $Q_c^{-1} = 0.1$. (For interpretation of the references to color in this figure legend, the reader is referred to the web version of this article.)

**Table 2**

Number of events characterized by a signal-to-noise ratio (SNR) of the envelope in the coda window higher than five. We assessed this ratio at the three most significant frequency bands: 2–4 Hz, 4–8 Hz and 12–24 Hz. For Pollino and MSH dataset almost all the waveforms are characterized by a high SNR of the coda envelope. On the contrary, Vrancea dataset shows a low percentage of waveforms with SNR > 5, decreasing with increasing frequency.

| Coda signal to noise ratio > 5 | | | |
|---|---|---|---|
| Dataset | $n_{ev}/n_{tot}(\%)$ (2–4 Hz) | $n_{ev}/n_{tot}(\%)$ (4–8 Hz) | $n_{ev}/n_{tot}(\%)$ (12–24 Hz) |
| Pollino | 896/911 (98.4%) | 899/911 (98.7%) | 878/911 (96.4%) |
| MSH | 442/447 (98.9%) | 446/447 (99.8%) | 447/447 (100%) |
| Vrancea | 205/333 (61.6%) | 124/333 (37.2%) | 92/333 (27.6%) |

A second test to examine whether the chosen coda window is in the diffusion regime is to calculate the transport mean free path $l_{tr}$ and compare it with the average epicentral distance of the events, $\langle r \rangle$ (Wegler, 2003). These equations are used in several applications of kernel-based coda imaging using the diffusion equation to separate scattering from absorption (e.g., Prudencio et al., 2017).

$$l_{tr} = \frac{d \cdot p}{V_S} \tag{6}$$

where $V_S$ is the average velocity of S-waves, $p$ is equal to $2\alpha$ (Eq. (2)) and $d$ is the diffusivity (Wegler and Lühr, 2001), At crustal and lithospheric scales, a more appropriate way to compute $l_{tr}$ is to consider multiple scattering (Eulenfeld and Wegler, 2016). The transport mean

free path $l_{tr}$ was computed using the multiple scattering coefficient $g^*$, obtained using the *Qopen* software from Eulenfeld and Wegler (2016), as $l_{tr} = 1/g^*$.

*Qopen* was developed for intrinsic and scattering attenuation separation by using the effect of the two different mechanisms on the shape of the waveform envelope. Assuming acoustic isotropic scattering, the energy density (envelope) at a certain frequency was modelled by

$$E_{mod}(t, \mathbf{r}) = WR(\mathbf{r})G(t, \mathbf{r}, \mathbf{g})e^{-bt} \tag{7}$$

where $W$ is the spectral source energy, $R(\mathbf{r})$ is the energy site amplification factor, $e^{-bt}$ is the exponential intrinsic damping with time, depending on the intrinsic absorption parameter $b$ and $G$ is the Green's function, approximated by the 3D isotropic radiative transfer theory solution of Paasschens (1997). The modelled energy envelope is then compared to observed energy envelopes at different seismic stations by minimizing an error function which expresses the difference of the logarithms of the observed and modelled envelopes. This is done by optimizing $\mathbf{g}$, the scattering parameters. The resulting system of equations is solved by means of least-squares for $\mathbf{g}$, $b$, $R$ and $W$. $\mathbf{g}$ is approximated by the scattering coefficient $g0$ in the Paasschens (1997) solution. In real media, isotropic scattering is not a valid assumption and therefore $g0$ in this case is interpreted as the transport scattering coefficient $g^*$.

Being in the diffusion regime requires that $\langle r \rangle \gg l_{tr}$. The distribution of epicentral distances varies significantly between the three datasets (Fig. 5) and the weighted average of each of them, which is considered
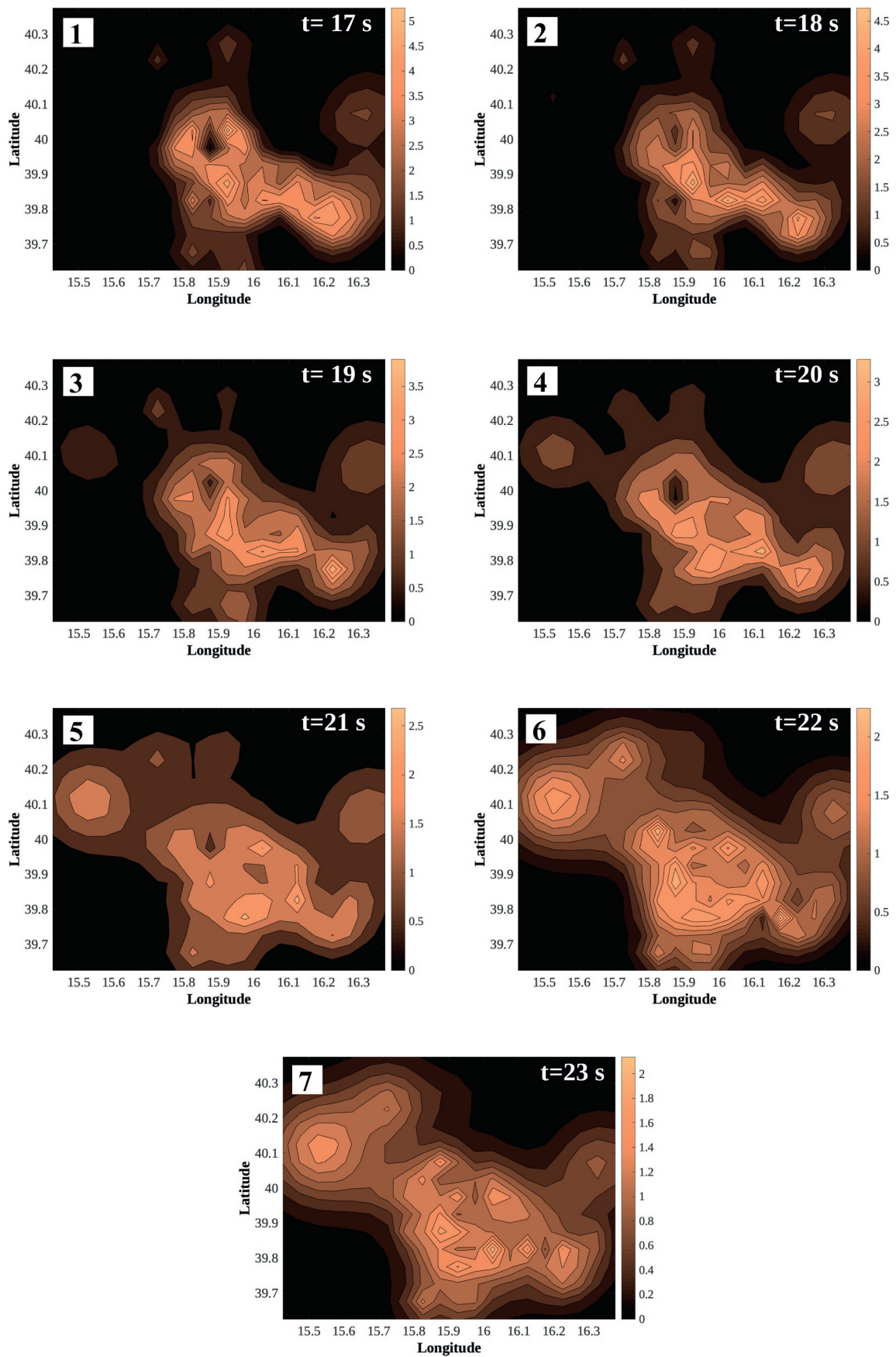
**Fig. 8.** Normalized energy density variations for the Pollino area using kernel $F1$ for each coda sub-window. Light colours indicate high energy density while darker colours indicate lower energy density. The lapse time for each window is also shown. (For interpretation of the references to color in this figure legend, the reader is referred to the web version of this article.)
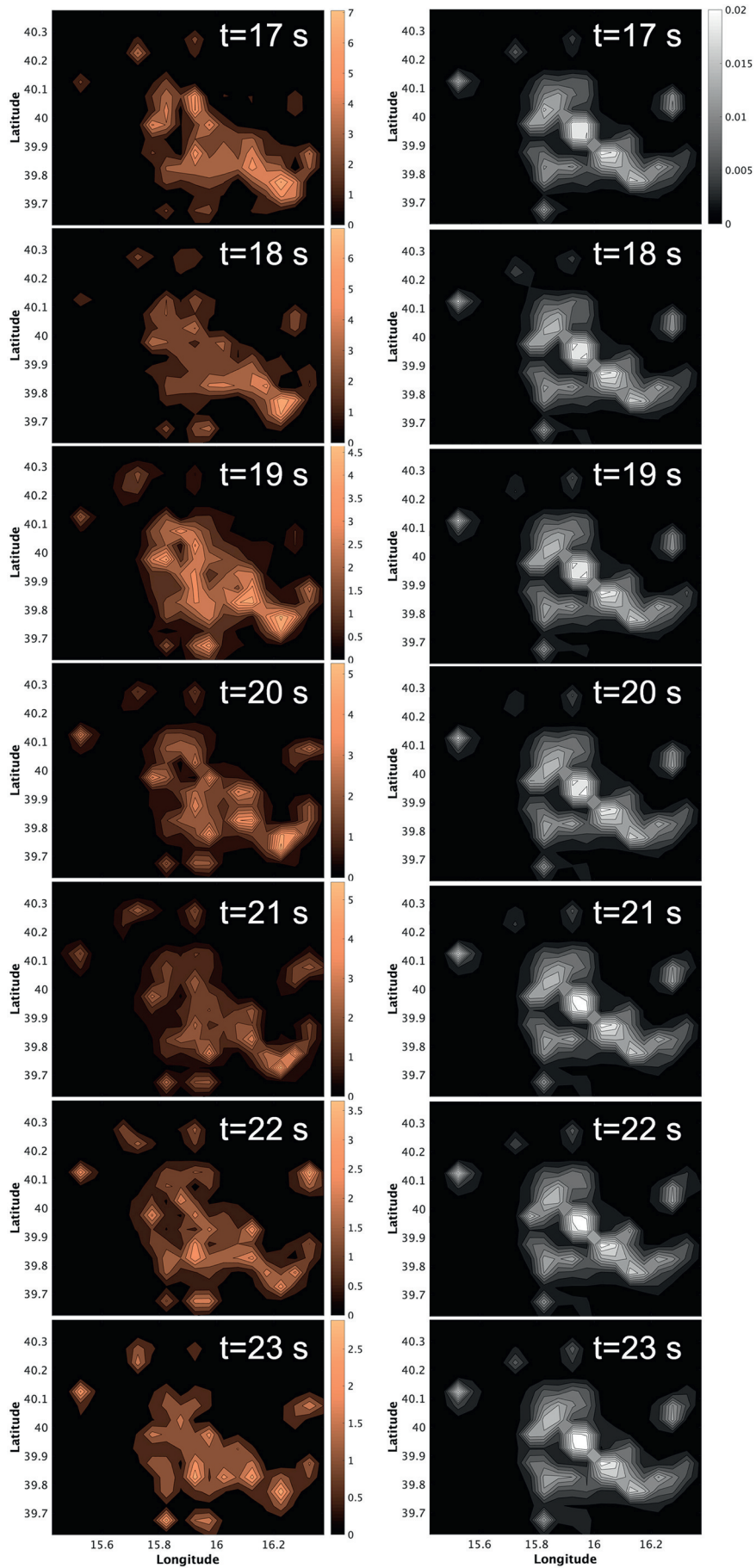
*(caption on next page)*

**Fig. 9.** Normalized energy density variations for the Pollino area using kernel *F*2 (left panels) and corresponding checkerboard tests for each coda sub-window (right panels). Light colours indicate high energy density while darker colours indicate lower energy density. (For interpretation of the references to color in this figure legend, the reader is referred to the web version of this article.)

more reliable then the standard average, was used for this purpose. For Pollino, the transport mean free path $l_{tr}$ was calculated for a source-station pair at an average epicentral distance of 19.6 km ($\langle r \rangle$) to be approximately 12 km, showing that the diffusion regime is reached in this area.

*3.3. Measuring coda attenuation by linearization and a non-linear approach*

The next step of the procedure to obtain the $Q_c^{-1}$ values is to compute the envelope of each waveform using a Hilbert transform at different frequency bands whose extreme values are at one-third of the central frequency, *cf* (Table 1). A waveform example and its associated envelope for each dataset are shown in Fig. 6. The obtained envelopes are smoothed using a moving window which depends on the central frequency as *nf/cf* (see Table 1). $Q_c^{-1}$ values can be obtained using a *linear* (e.g., Calvet et al., 2013 ; De Siena et al., 2016) or *non-linear* approach (e.g., Ibáñez et al., 1993; Menke, 2012). The former consists of taking the natural logarithm of Eq. (2) (Aki and Chouet, 1975)

$$\frac{\ln[E(f, t)t^\alpha]}{2\pi f} = \frac{\ln[S(f)]}{2\pi f} - \frac{1}{Q_c}t \tag{8}$$

Fitting a straight line to the data, we correlate $\frac{\ln[E(f,t)t^\alpha]}{2\pi f}$ and time *t*, with a gradient equal to $-\frac{1}{Q_c}$ (Calvet and Margerin, 2013).

An alternative approach is to estimate $Q_c$ using a *non-linear* method, e.g. a *grid search algorithm*, which consists of searching in a pre-defined list of $Q_c^{-1}$ values for the one that minimizes the residual between the observed energy (obtained directly from the waveform at a fixed frequency) and the predicted energy (calculated through substituting the $Q_c^{-1}$ value into Eq. (2)). An example of a misfit plot showing the range of model parameters examined by a grid search algorithm with their associated residual is shown in Fig. 7a.

The main advantage of using a linear approach is that it is easy to implement and the problem can be solved using a simple form of regression such as linear least-squares. However, if the problem under investigation is non-linear we need to make some assumptions to linearize it: the linearized data parameters are assumed to be normally distributed, independent random variables with a uniform variance (Menke, 2012). Therefore, the data distribution in its original form must have a log-normal distribution. Also, in the case of the presence of outliers in the data, this approach gives a result that is heavily biased by them. Using a grid-search method, the presence of outliers could cause a misfit plot without a single minimum and this will result in an anomalous model parameter (Fig. 7b). The main advantages of using a grid-search method are that it is relatively easy to implement and it considers every possible solution in the pre-defined parameter space, selecting the one with the smallest residual. Even though this method gives a solution that is closer to the real one (Menke, 2012), the computational time increases with the increase of the size of the list of possible parameter values.

Ibáñez et al. (1993) demonstrate that the two approaches give similar results when the signal-to-noise ratio in the coda window is higher than five. If the ratio is lower than five, the linear method tends to overestimate $Q_c^{-1}$. Table 2 summarizes the average $Q_c^{-1}$ values obtained for the three datasets using both a linear and a non-linear approach.

*3.4. Absorption tomography (AT)*

Until now, researchers have obtained the $Q_c$ structure of various study areas by either of the two methods, M0 and (more recently) M1,

described in Sections 2.1 and 2.2, respectively. Still, the quantity that they measure and that all sensitivity kernels model in space is seismic energy (the envelope) not $Q_c$. Here, we propose an alternative approach, hereafter called absorption tomography (AT), joining the potential of single scattering tomography (Nishigami, 1991) with that of Multiple Lapse Time Window Analysis (MLTWA) (Del Pezzo and Bianco, 2010; Fehler et al., 1992).

The first step of the analysis is assessing the number and spatial distribution of sources and receivers, which allows to select the parametrization and number of the nodes (*P*) of the grid in which the area will be divided. Having chosen a suitable starting lapse time $t_W$ and length of coda window $L_W$ (see Section 3.2), we divided the filtered energy envelopes of each waveform into *N* sub-windows of length $L_W/N$. For each waveform, the energy of each of the $N-1$ sub-windows, $E^i(t_k)$, has been normalized by the energy of the $N^{th}$ window, $E(t_N)$

$$\widetilde{E}^i(t_k) = \frac{E^i(t_k)}{E^i(t_N)} \tag{9}$$

where $k = 1,...,N-1$ is the index of the sub-window, $i = 1,...,M$ is the index of the waveform, and $t_N$ is the normalization window. Dividing the energy of each window with the energy of the last window, as described, is a form of late coda normalization and it is essential in order to remove any source and site variations effects from our data (Sato et al., 2012).

In order to map the absorption at each block *P*, we use the sensitivity kernels described by both Eqs. (3) and (5): we then performed $N-1$ inversions, for each sub-window $t_k$, of the equation

$$\widetilde{E}^i(t_k) = \sum_{j=1}^{P} F_{ij}\widetilde{E}_j(t_k) \quad \text{for} \quad i = 1, ...,M \tag{10}$$

where $F_{ij}$ is the sensitivity kernel associated to the $i^{th}$ waveform computed at the $j^{th}$ node of the grid (either *F*1 or *F*2, Figs. 1 and 3), and $\widetilde{E}_j(t_k)$ represents the normalized energy at the $j^{th}$ node for the $k^{th}$ sub-window. Different numbers of sub-windows were tested and they all give similar results (Figs. S3, S4 and S5) in the Supplementary material for the three datasets).

This equation is solved as an inverse problem **d** = **Gm**. $N-1$ inverse problems (equal to the number of sub-windows) are solved, in which the elements of the data vector are the normalized energy values stated in Eq. (9), $\mathbf{d} = [\widetilde{E}^1(t_k), \widetilde{E}^2(t_k), ...,\widetilde{E}^M(t_k)]$ and the elements of the **G** matrix are the sensitivity kernels $F_{ij}$. The inversion results in a vector **m** composed of the normalized energy values of the $k^{th}$ window $t_k$ at all the *P* nodes of the grid $\mathbf{m} = [\widetilde{E}_1(t_k), \widetilde{E}_2(t_k), ...,\widetilde{E}_P(t_k)]$. The inverse problem is solved using a zeroth-order Tikhonov regularization. The matrix form of Eq. (10) is

$$\begin{bmatrix} \widetilde{E}^1(t_k) \\ \widetilde{E}^2(t_k) \\ \vdots \\ \widetilde{E}^M(t_k) \end{bmatrix} = \begin{bmatrix} F_{11} & F_{12} & ... & F_{1P} \\ F_{21} & F_{22} & ... & F_{2P} \\ \vdots & \vdots & \ddots & \vdots \\ F_{M1} & F_{M2} & ... & F_{MP} \end{bmatrix} \begin{bmatrix} \widetilde{E}_1(t_k) \\ \widetilde{E}_2(t_k) \\ \vdots \\ \widetilde{E}_P(t_k) \end{bmatrix} \tag{11}$$

By using *F*2, the inversion matrix changes for each lapse time. Figs. 8 and 9 show the energy variations for each coda sub-window for the Pollino area with the two kernels.

Theoretically, the values of energy at each node should form a decreasing curve which can be modelled by Eq. (2). Thus, a $Q_c^{-1}$ value for each node is obtained by either a linear approach using Eq. (8), or finding, from a pre-defined set of values, the $Q_c$ that minimizes the residuals between the observed energy values at each node and the predicted ones obtained using Eq. (2). The latter method is the so-called grid search method. The final result is a map of $Q_c^{-1}$ values which
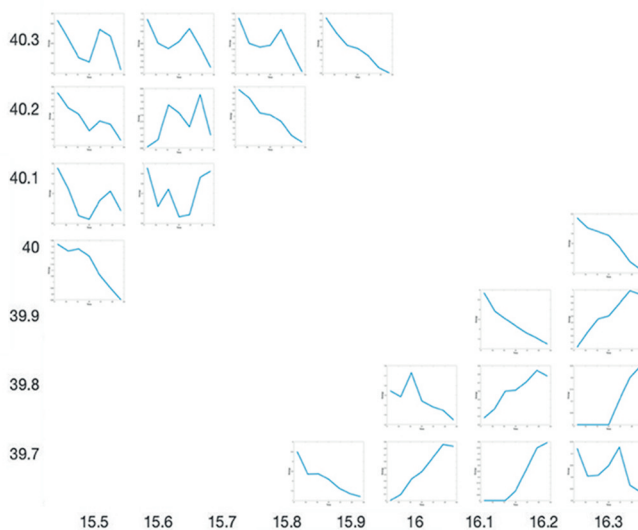
**Step 1:** Divide the coda window of the filtered energy envelopes into N smaller windows.
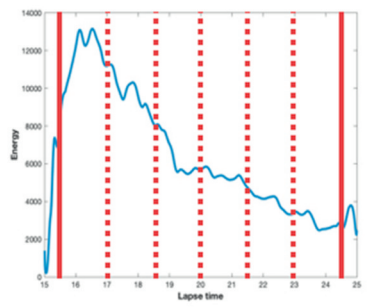


**Step 2:** Calculate the energy for each window normalized by that of the last window.
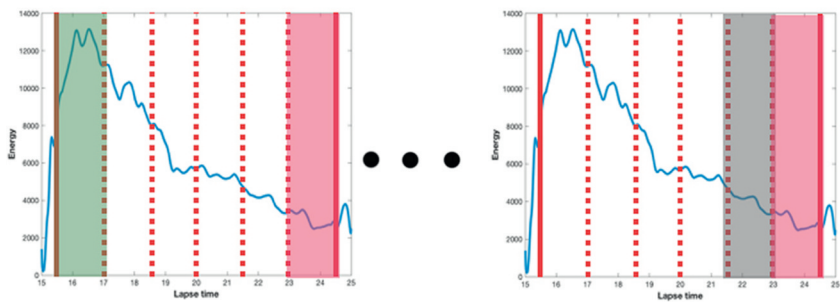


**Step 3:** Map in space the energy of the N-1 time windows for all source-station pairs using the sensitivity kernels



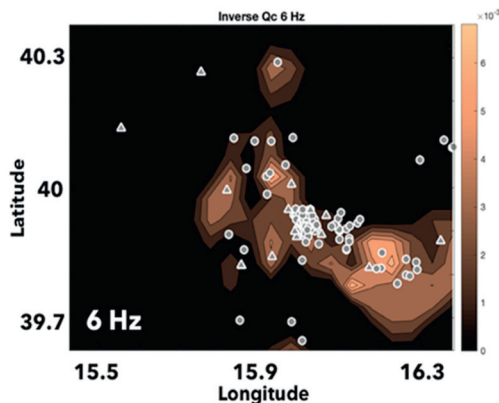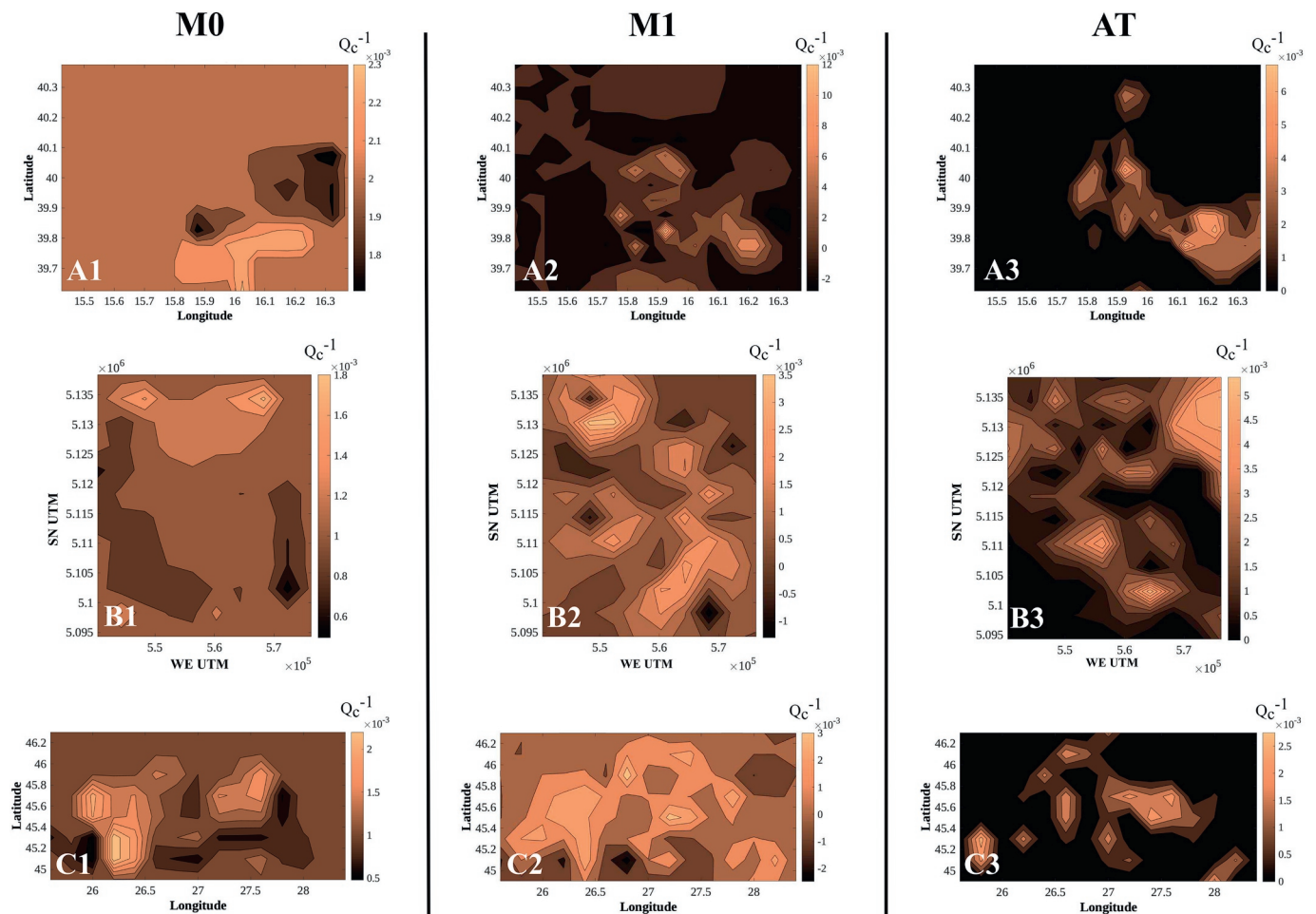**Step 4:** Estimate a single Qc⁻¹ value for each node and plot them on map.



**Fig. 10.** A sketch to clarify the steps that lead to the final model in AT.

**Fig. 11.** $Q_c^{-1}$ maps in the 4–8 Hz frequency band of: Pollino area (panels A1–A3), MSH (panels B1–B3) and Vrancea (panels C1–C3). The left panels (A1, B1 and C1) show the resulting maps obtained using the regionalization approach (M0), the central panels (A2, B2 and C2) show the maps obtained with standard coda attenuation imaging using diffusive sensitivity kernels (M1) and the right panels (A3, B3 and C3) show the maps obtained using the proposed spatial coda intensity modelling methodology (AT).

represent the spatial variations of seismic absorption using AT. The sketch in Fig. 10 clarifies the steps of the procedure from the selection of windows in the envelope to the final absorption model obtained.

### 3.5. Mapping strategy

In the following, we describe the mapping strategies followed for each of the three study areas. Independently of the mapping strategy, having obtained the $Q_c$ values at each node, we always use a filled contour plot to map these values with the palette ranging from darker colours (low $Q_c^{-1}$ and thus low absorption) to brighter colours (high $Q_c^{-1}$ and thus high absorption).

#### 3.5.0.1. Pollino area mapping
We applied AT and compared it to the results obtained using M1 and M0, dividing the area into blocks of size 7 km × 5.6 km, in five frequency bands: 2–4 Hz, 4–8 Hz, 6–12 Hz, 8–16 Hz, and 10–20 Hz. The number of waveforms, 911, and their distribution in space allow us to use a fine grid spacing (320 blocks), where our inverse problem is over-determined. Fig. 11 (top panels from A1 to A3) show the results obtained using the three techniques in the 4–8 Hz frequency band.

#### 3.5.0.2. Mount St. Helens mapping
We applied AT and compared it with the results obtained using M1 and M0, dividing the area into blocks of size 4 km × 5 km, in five frequency bands: 2–4 Hz, 4–8 Hz, 6–12 Hz, 8–16 Hz, 10–20 Hz and

12–24 Hz. The number of waveforms, 447, and the number of blocks in the grid, 120, make the inverse problem over-determined. Fig. 11 (middle panels from B1 to B3) show the results in the 4–8 Hz frequency band.

#### 3.5.0.3. Vrancea mapping
As in the previous two datasets, Fig. 11 (bottom panels from C1 to C3) show the comparison between the results obtained using M0, M1 and AT, respectively, by dividing the area into blocks of size 22 km × 22 km, in the 4–8 Hz frequency band.

### 4. Results and discussion

In Fig. 11, we present the $Q_c^{-1}$ maps, obtained using a non-linear approach, for the three datasets (A: Pollino, B: MSH, C: Vrancea) using regionalization (M0, left column), coda attenuation imaging using sensitivity kernels (M1, central column) and absorption tomography with kernel $F1$ (AT, right column). The difference between the maps obtained using M0 and M1 is evident. Using regionalization, if a block is crossed by a given amount of rays, each one bringing a different value of $Q_c^{-1}$ with a significant overall variation, averaging over those values causes all the information regarding this contrast to vanish. Moreover, smoothing the distribution of $Q_c^{-1}$ in space over their nearest neighbours, the resulting map will show a very low-contrast variation of absorption, unless some blocks are crossed by rays carrying similar information. This is clear in Fig. 11, panels A1 and B1 for Pollino and

**Input**   **Output (M1)**   **Output (AT)**
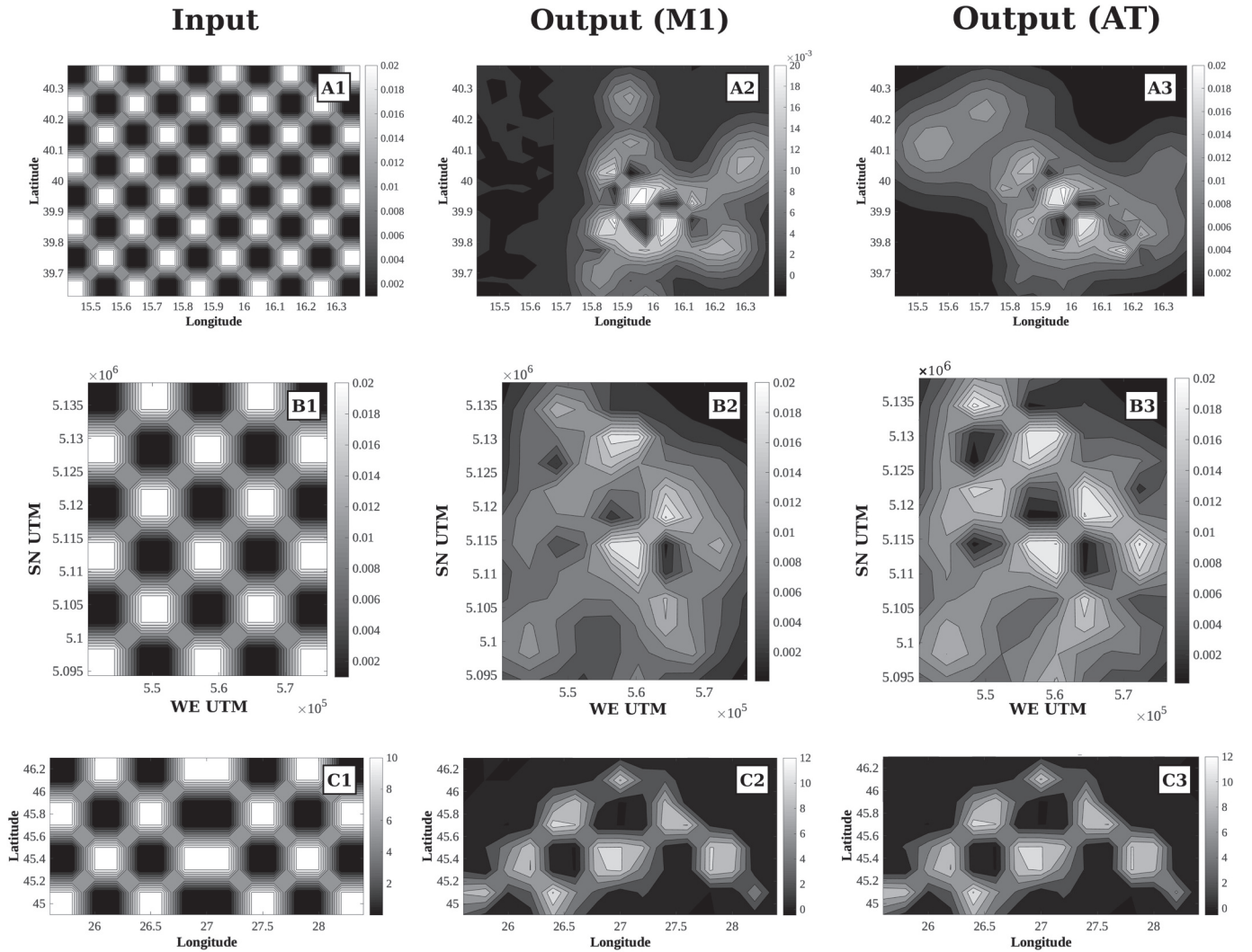


**Fig. 12.** Checkerboard tests performed for the three datasets for the two different inversion techniques (M1 and AT). Upper panels show the input and the two outputs of the checkerboard test for the Pollino area. Middle panels show the input and outputs of the checkerboard test for MSH volcano and the lower panels show the input and outputs for Vrancea. The lapse time windows for the panels on the right are 23 s, 33 s and 38 s for Pollino, MSH and Vrancea respectively.

MSH datasets respectively. In both datasets the ray coverage is high in the centre of the map (Fig. 4a and b), where no significant variation of $Q_c^{-1}$ is observed. At the edges of these maps, some low and high absorption patterns appear, where fewer rays with likely similar information cross each block. The Vrancea dataset has the fewest number of waveforms between the three datasets (Fig. 4c) for the largest study area. In Fig. 11, panel C1, more variations all over the map are visible. As mentioned earlier, these variations are likely caused by rays carrying similar information, although the number of rays crossing each block is on average lower than the other two datasets, making the contribution of each waveform to the average $Q_c^{-1}$ value in each block more important.

The introduction of sensitivity kernels (methodology M1) allows for a better representation of localized absorption variations, as shown in the second column of Fig. 11. The difference in this case is that while a $Q_c^{-1}$ value is still obtained for each waveform, by inverting for the spatial distribution of the absorption anomalies using sensitivity kernels, the higher contribution of the areas around the source and the receiver is taken into account (Del Pezzo et al., 2016). Synthetic testing was performed to assess the resolution of the resulting maps (Fig. 12) and allows for an interpretation of the main patterns.

The right column in Fig. 11 shows the results of the AT methodology using kernels *F*1. As M1, AT overcomes the main approximations of M0:

the $Q_c^{-1}$ value for a waveform is not constant along the whole ray path and representative of the averaged crustal properties of the blocks crossed by each source-receiver ray. Therefore, the resulting map gives you information in areas where theoretically should not be any. AT improves M1 by applying the sensitivity kernels to the energy measurements recorded at the station (not directly to $Q_c^{-1}$), then measuring absorption at each node in space. It also implements a lapse-time dependent procedure that takes more properly into account the variations of scattering across the data and allows implementing the lapse-time-dependent kernels *F*2. The most striking difference compared to the maps obtained with the other two methodologies is that the absorption anomalies are more localized since different $Q_c^{-1}$ values are obtained by inverting for each node in space. By first inverting for the distribution of energy in space for each time window, as described in Section 3.4, the positivity constraint is automatically implemented.

Fig. 13 shows that for the Pollino area dataset, the nodes characterized by zero energy are distributed in the areas not crossed by any rays. Parts of the area which have $Q_c^{-1} = 0$ using AT appear to have positive values when M1 is applied. Moreover, M1 returns negative $Q_c^{-1}$ also in zones where the ray coverage is adequate to recover the absorption structure (Fig. 13, bottom right panel in box). A checkerboard test was performed for the inversion of each time window; however, these cannot be directly compared to the checkerboard tests of the M1
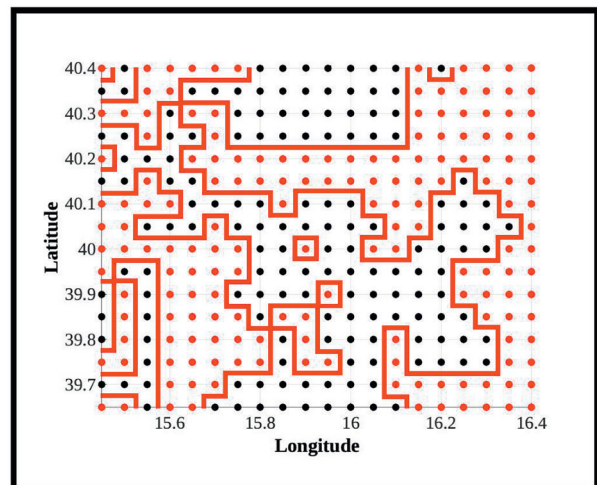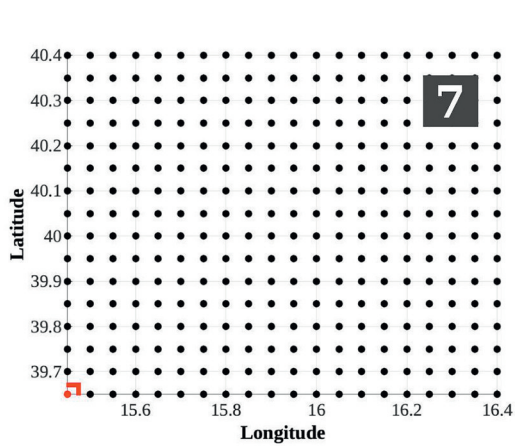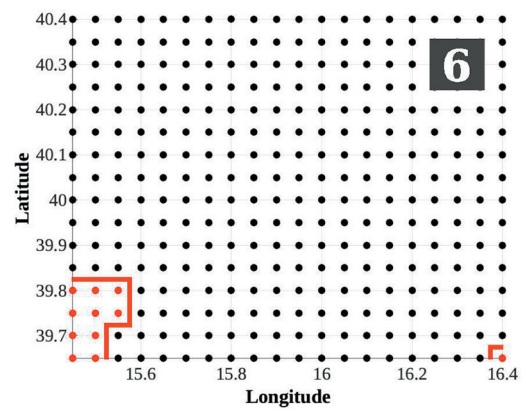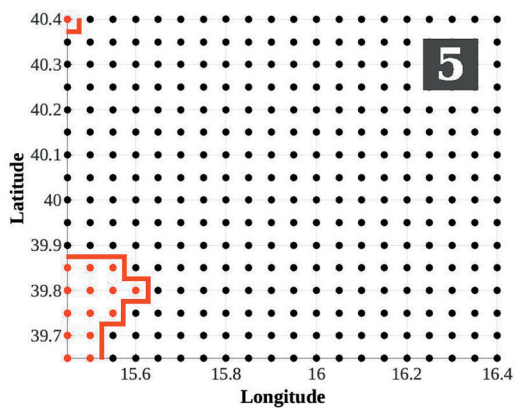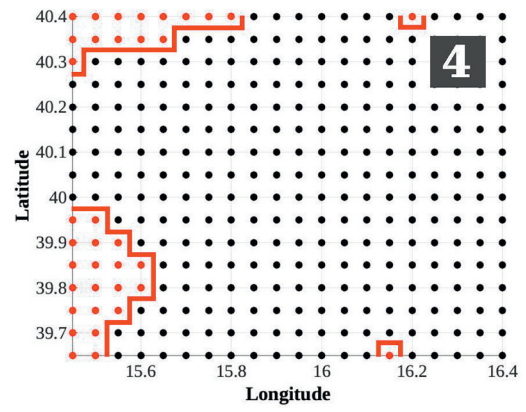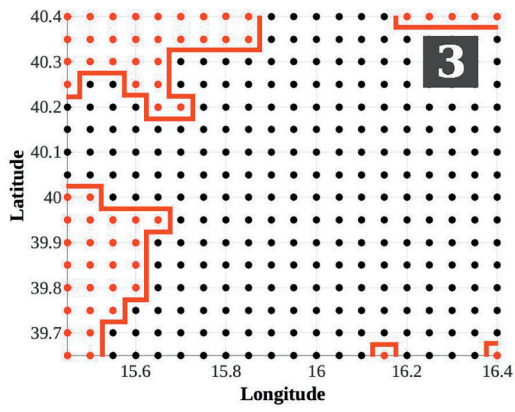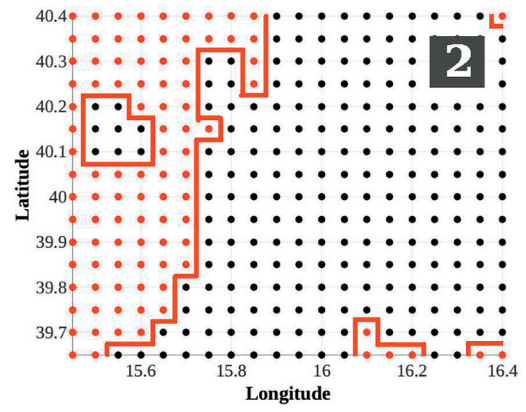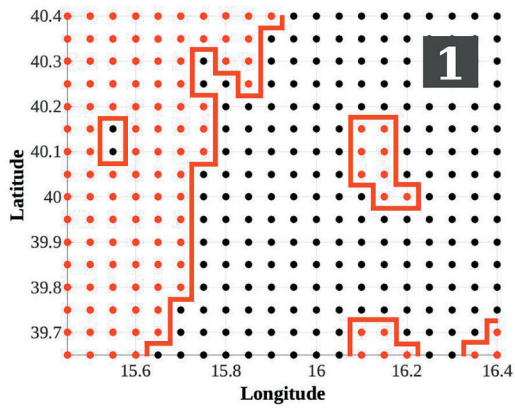
*(caption on next page)*

**Fig. 13.** Panels from 1 to 7, nodes characterized by zero values (red points) and greater than zero (black points) obtained using AT methodology at 6 Hz for each coda sub-window. The boxed bottom right panel shows nodes characterized by negatives (red points) and greater than zero (black points) using M1 methodology at 6 Hz. We may obtain negatives also where the ray coverage is not low, while using the AT methodology we obtain zeroes only in blocks crossed by no rays. (For interpretation of the references to color in this figure legend, the reader is referred to the web version of this article.)

**Table 3**
Average inverse $Q_c$ values and relative standard deviation calculated for the three datasets (first column) computing a linear and a non-linear approach for $M0$ and $M1$ methodology (Panel (A)) and for AT methodology (Panel (B)). $Q_c^{-1}$ for Vrancea in the bottom right corner of the table is marked with an asterisk because it has been obtained by removing some outliers that clearly altered the result [Average $Q_c^{-1}$ (no outliers) = 0.0098 ± 0.0200].

| | (A) M0 and M1 methodology | | (B) AT methodology | |
| | Linear approach | Non-linear approach | Linear approach | Non-linear approach |
|---|---|---|---|---|
| Dataset | $Q_c^{-1} \pm \sigma$ | $Q_c^{-1} \pm \sigma$ | $Q_c^{-1} \pm \sigma$ | $Q_c^{-1} \pm \sigma$ |
| Pollino | 0.0059 ± 0.0019 | 0.0020 ± 0.0011 | 0.0035 ± 0.0026 | 0.0022 ± 0.0017 |
| MSH | 0.0024 ± 0.0010 | 0.0014 ± 0.0009 | 0.0024 ± 0.0014 | 0.0023 ± 0.0015 |
| Vrancea | 0.0038 ± 0.0008 | 0.0012 ± 0.0007 | 0.0029 ± 0.0014 | 0.0023 ± 0.0015* |

methodology because of the different model parameters of the inverse problem. We can instead compare the checkerboard test of each sub-window with each other to asses how the recovery of the absorption structure changes with lapse time.

A summary of the average $Q_c^{-1}$ values obtained with both a linear and a non-linear approach (grid search method) is shown in Table 3. The signal-to-noise ratio of the coda window for each dataset was assessed (see Table 2. For the M0 and M1 methodologies, the linear approach over-estimated $Q_c^{-1}$ for every dataset. The difference is most pronounced in Vrancea. Taking into account the standard deviation, the $Q_c^{-1}$ values for Pollino and MSH overlap. Using the AT methodology, the linear approach again overestimates $Q_c^{-1}$ but the discrepancy between the linear and non-linear approach is less for all the datasets. However, for Vrancea this average is evaluated without taking into account the presence of outliers, which occur from the dataset. In this case, there is no minimum in the misfit curve of the grid-search method and anomalous values of $Q_c^{-1}$ arise (Fig. 7). These irregular $Q_c^{-1}$ values are not as visible when using linearization, which tends to average abrupt changes.

The two main assumptions which may limit the applicability of AT are: (1) the diffusion regime approximation and (2) energy leakage into the upper mantle. The first assumption has been discussed in Section 2.2. It is worth noting that while being in the diffusion regime requires that $\langle r \rangle \gg l_{tr}$, in our case $\langle r \rangle > l_{tr}$. Regarding the second limitation of AT, energy leakage from the crust into the mantle needs to be taken into account in order not to overestimate $Q_c$. According to Margerin et al. (1998)

$$Q_c^{-1} = Q_i^{-1} + Q_l^{-1} \qquad (12)$$

where $Q_l$ is the leakage quality factor. In thin crustal layers of thickness $H$ where $H \approx l_{tr}$, the effectiveness of energy leakage is maximum (Del Pezzo and Bianco, 2010; Margerin, 2017). Sanborn et al. (2017) developed the computer code RADIATIVE3D, whose first application was in Sanborn and Cormier (2018), for seismic radiative transport modelling using a flexible Earth model and source mechanisms. The implementation of this code in future analysis could allow to take into account the effect of energy leakage due to the variation of crustal thickness in the study areas.

### 4.1. AT with lapse-time dependent sensitivity kernels and comparison

As mentioned in Section 2.2, the sensitivity kernels used for mapping the spatial distribution of $Q_c^{-1}$ with both M1 and AT methodologies are approximate analytical functions which do not depend on lapse time, derived by Del Pezzo et al. (2016). This form of diffusive sensitivity kernel is not the optimum choice to define the lapse-time sensitivity of the coda in our study areas, as they have only been proven effective for active (Del Pezzo et al., 2016) or shallow (De Siena et al.,

2017) seismicity and in volcanic areas. Nevertheless, as a preliminary test and to understand if the dataset is adequate for the procedure, we recommend using kernels $F1$: the sequential AT inversion code with $F1$ runs in ~ 1 min on a standard Macbook Pro (Late 2013) for each of the three areas. Defining the forward problem with $F2$ increased the AT computation time to over three hours at Pollino on the same machine. With wider datasets the application of $F2$ will likely require parallelization of the codes. The AT technique with kernels $F1$ clearly showed that AT does not improve illumination in Vrancea compared to M1 (Fig. 12, lowest panels), thus we avoid the computational effort of implementing $F2$.

The lapse-time-dependent multiple-scattering kernels $F2$ is a physically more meaningful approach than kernels $F1$. AT is ideally suited to implement these compressed lapse-time-dependent 3D kernels in a tomographic procedure. In the case of Pollino, Fig. 9 shows the energy variations for each coda sub-window (left) and the corresponding increase in illumination (right, checkerboard test) by using $F2$. The figure shows the slightly reduced illumination and resolution on structures compared to the analytic $F1$ kernels (Fig. 12, upper right panel). This is a consequence of the reduced focus on the line connecting source and receiver of kernels $F2$, which offer increased lateral illumination at late lapse time and at the source and station locations.

Apart from the computational effort, in order to obtain $F2$ we have to pre-set the average scattering and absorption parameters of the area. A preliminary analysis with MLTWA (Carcolé and Sato, 2010; Fehler et al., 1992) can help reducing uncertainty on these parameters. A more refined approach is the one proposed by e.g., Ogiso (2018) for the separate estimation of absorption and scattering parameters in 3-D space based on envelope-fitting, back-projection in a vertically-varying velocity model, and sensitivity kernels computed on a 1-D velocity structure. While the method theoretically allows to invert for both scattering and absorption, other authors have observed that the trade-off between these parameters, due to their relation to both correlation length and velocity fluctuation, could make a separate tomographic estimate unreliable (Del Pezzo et al., 2016; Sato et al., 2012; Takeuchi, 2016). By focusing on the late part of the envelope and checking for the onset of diffusion experimentally we try to remove this bias, focusing on absorption only.

All these considerations are necessary when we intend to interpret the anomalies in terms of Earth structures and geology. Apart from the methodology and its limitations per se, the coverage of the dataset is critical to obtain reliable structures. An appropriate pre-processing of the data in terms of the location of the events, the accurate picking of P- and, whenever possible, S-wave arrivals and a high signal-to-noise ratio for each waveform are necessary to obtain reliable results. Fig. 4 shows the three different datasets used in this study. Going from Pollino area in Fig. 4a to Vrancea in Fig. 4c, it is evident that the ray density decreases abruptly. However, in MSH (Fig. 4b) even if the ray density does
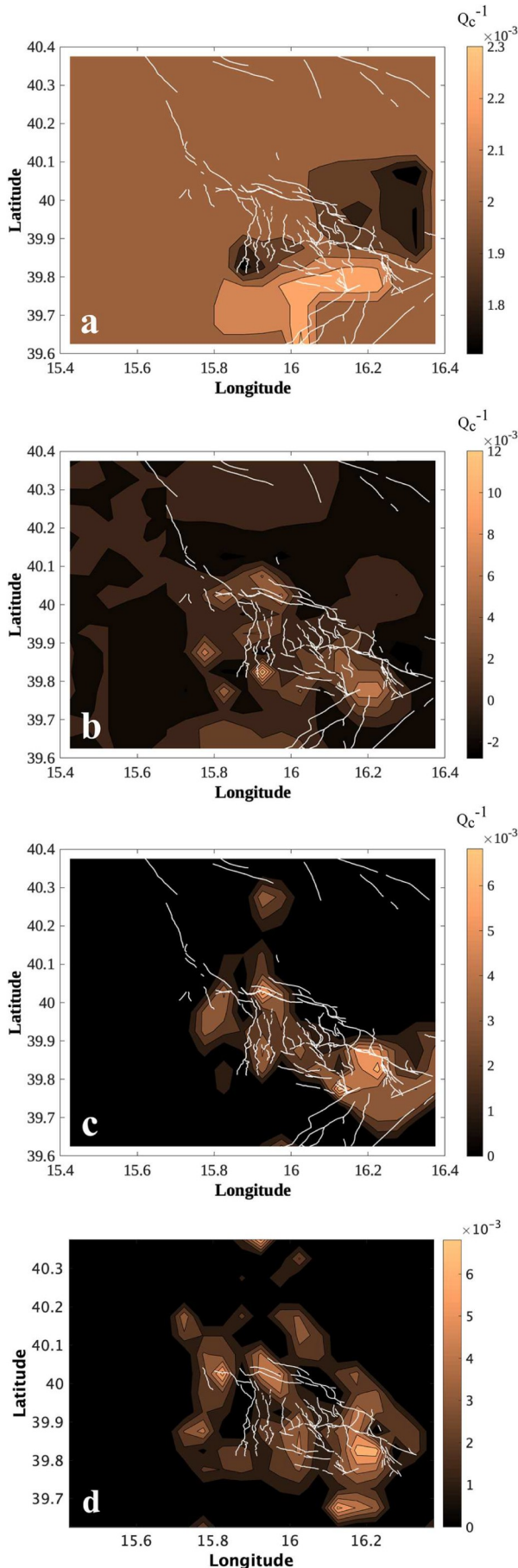
**Fig. 14.** 2D Absorption maps in the 4–8 Hz frequency band for the Pollino area obtained using: (a) a regionalization approach (M0) (b) standard coda attenuation imaging using sensitivity kernels (M1), and AT using kernels *F*1 (c) and (d) *F*2. We overlay the faults of the area (white colour) by Brozzetti et al. (2017) .

not seem as high as in the Pollino area, the spatial distribution of sources and receivers still allows an interpretation of the resulting image. On the contrary, when the coverage is not satisfactory and the number of waveforms is not sufficient, such as in Fig. 4c, the map cannot be reliable enough for interpretation.

If the dataset fulfills all the requirements, as in the case of the Pollino area, the absorption map obtained using AT allows for a more reliable interpretation of the main patterns in terms of geological and geophysical features of the area. In Fig. 14, we compare the image obtained using M0 (Fig. 14a), M1 (Fig. 14b) and AT methodologies with kernels *F*1 and *F*2 (Fig. 14c, d). Using M0 (a), some absorption anomalies are observed in part of the fault areas but the overall absorption structure does not follow the fault network. The correlation becomes clearer using M1 (b), and dramatically improves when using the AT methodology with *F*1 (c). Both M1 (b) and AT (c) recover the main high absorption patterns but AT better focuses on the faults by overcoming the single-$Q_c$-value approximation for each source-receiver pair.

The progressive improvement from technique M0 to AT kernels (*F*1) is dramatic, with ghosts removed west, north, and north-east of the SE-NW-trending fault region. The implementation of proper multiple-scattering lapse-time kernels (*F*2-d) reduces focus across the faults due to the reduced kernel sensitivity between sources and stations. This reduction, already observed in volcanic areas (Akande et al., 2019), is compensated by a time-dependent forward model that takes into better account the physics underlying scattering processes.

## 5. Conclusions

We proposed a novel technique for absorption mapping, based on the ideas of scattering tomography and MLTWA, and compared it with the existing methodologies which make use of regionalization and sensitivity kernels for a diffusive regime. While the existing techniques calculate a $Q_c^{-1}$ value for each waveform and map it in space, our methodology uses diffusive sensitivity kernels to invert for the spatial distribution of energy as a function of lapse time and obtaining a $Q_c^{-1}$ value for each node of the pre-defined grid. We applied the aforementioned methodologies (M0, M1 and AT) to data from three different settings: the Pollino fault network (Southern Italy), Mount St. Helens volcano (USA) and Vrancea (Romania). At Pollino, we also applied time-lapse-dependent sensitivity kernels, which, although more computationally expensive, allow for a proper forward modelling of the scattering process.

Imaging using regionalization does not result in a reliable representation of the absorption variations, even when the number of waveforms and ray crossing are significant. Its lack of a physical forward model forbids a reliable testing of the anomalies and its averaging process smooths contrasts. The introduction of diffusive sensitivity kernels in a tomographic framework improves illumination obtained using regionalization, provides a forward model that can be implemented and tested in tomographic imaging, and allows for a more realistic recovery of the absorption variations. Still, this forward model describes the sensitivity of energy to space in time, while coda attenuation is measured on single-station data for the entire time period.

The proposed AT methodology using late time-lapse-dependent sensitivity kernels redistributes energy in space to then measure absorption, better highlighting localized variations and automatically implementing a non-linear positivity and selection constraint. Using a high-quality dataset (Pollino), the improvement introduced by AT in

highlighting the main geological features of the area is evident if compared with M0 and, to a lesser degree, M1, independently of the kernels used. If appropriate kernels are available and the bias between scattering and absorption parameters are independently resolved, AT can potentially be developed as a full scattering and absorption imaging method in single-layer media with single scattering, multiple scattering and diffusive properties.

## Data availability

The Mount St. Helen's dataset is available on IRIS (www.iris.edu). The Pollino area and Vrancea datasets are available upon request.

## Declaration of Competing Interest

The authors declare that they have no known competing financial interests or personal relationships that could have appeared to influence the work reported in this paper.

## Acknowledgments

## Appendix A. Supplementary data

Supplementary data to this article can be found online at https://doi.org/10.1016/j.pepi.2019.106337.

## References

Akande, W.G., De Siena, L., Gan, Q., 2019. Three-dimensional kernel-based coda attenuation imaging of caldera structures controlling the 1982–84 Campi Flegrei unrest. J. Volcanol. Geotherm. Res.

Aki, K., 1980. Attenuation of shear-waves in the lithosphere for frequencies from 0.05 to 25 Hz. Phys. Earth Planet. Inter. 21, 50–60.

Aki, K., Chouet, B., 1975. Origin of coda waves: source, attenuation, and scattering effects. J. Geophys. Res. 80, 3322–3342.

Borleanu, F., De Siena, L., Thomas, C., Popa, M., Radulian, M., 2017. Seismic scattering and absorption mapping from intermediate-depth earthquakes reveals complex tectonic interactions acting in the Vrancea region and surroundings (Romania). Tectonophysics 706, 129–142.

Brozzetti, F., Cirillo, D., de Nardis, R., Cardinali, M., Lavecchia, G., Orecchio, B., Presti, D., Totaro, C., 2017. Newly identified active faults in the Pollino seismic gap, southern Italy, and their seismotectonic significance. J. Struct. Geol. 94, 13–31.

Calvet, M., Margerin, L., 2013. Lapse-time dependence of coda q: anisotropic multiple-scattering models and application to the Pyrenees. Bull. Seismol. Soc. Am. 103, 1993–2010.

Calvet, M., Sylvander, M., Margerin, L., Villase nor, A., 2013. Spatial variations of seismic attenuation and heterogeneity in the Pyrenees: coda q and peak delay time analysis. Tectonophysics 608, 428–439.

Carcione, J.M., 2000. A model for seismic velocity and attenuation in petroleum source rocks: an acoustic model for petroleum source rocks. Geophysics 65, 1080–1092.

Carcolé, E., Sato, H., 2010. Spatial distribution of scattering loss and intrinsic absorption of short-period s waves in the lithosphere of Japan on the basis of the multiple lapse time window analysis of hi-net data. Geophys. J. Int. 180, 268–290.

De Siena, L., Del Pezzo, E., Thomas, C., Curtis, A., Margerin, L., 2013. Seismic energy envelopes in volcanic media: in need of boundary conditions. Geophys. J. Int. 195, 1102–1119.

De Siena, L., Thomas, C., Waite, G.P., Moran, S.C., Klemme, S., 2014. Attenuation and scattering tomography of the deep plumbing system of Mount St. Helens. J. Geophys. Res. Solid Earth 119, 8223–8238.

De Siena, L., Calvet, M., Watson, K.J., Jonkers, A., Thomas, C., 2016. Seismic scattering and absorption mapping of debris flows, feeding paths, and tectonic units at Mount St. Helens volcano. Earth Planet. Sci. Lett. 442, 21–31.

De Siena, L., Amoruso, A., Pezzo, E.D., Wakeford, Z., Castellano, M., Crescentini, L., 2017. Space-weighted seismic attenuation mapping of the aseismic source of Campi Flegrei 1983–1984 unrest. Geophys. Res. Lett. 44, 1740–1748.

Del Pezzo, E., Bianco, F., 2010. Two-layer earth model corrections to the mltwa estimates of intrinsic-and scattering-attenuation obtained in a uniform half-space. Geophys. J. Int. 182, 949–955.

Del Pezzo, E., Ibanez, J., Prudencio, J., Bianco, F., De Siena, L., 2016. Absorption and scattering 2-d volcano images from numerically calculated space-weighting functions. Geophys. J. Int. 206, 742–756.

Del Pezzo, E., De La Torre, A., Bianco, F., Ibanez, J., Gabrielli, S., De Siena, L., 2018. Numerically calculated 3d space-weighting functions to image crustal volcanic structures using diffuse coda waves. Geosciences 8, 175.

Eken, T., 2019. Moment magnitude estimates for central Anatolian earthquakes using coda waves. Solid Earth 10, 713–723.

Eulenfeld, T., Wegler, U., 2016. Measurement of intrinsic and scattering attenuation of shear waves in two sedimentary basins and comparison to crystalline sites in Germany. Geophys. J. Int. 205, 744–757.

Eulenfeld, T., Wegler, U., 2017. Crustal intrinsic and scattering attenuation of high-frequency shear waves in the Contiguous United States. J. Geophys. Res. Solid Earth 122, 4676–4690.

Fehler, M., Hoshiba, M., Sato, H., Obara, K., 1992. Separation of scattering and intrinsic attenuation for the Kanto-Tokai region, Japan, using measurements of s-wave energy versus hypocentral distance. Geophys. J. Int. 108, 787–800.

Havskov, J., Sørensen, M.B., Vales, D., Özyazıcıoğlu, M., Sánchez, G., Li, B., 2016. Coda q in different tectonic areas, influence of processing parameters. Bull. Seismol. Soc. Am. 106, 956–970.

Hennino, R., Trégourès, N., Shapiro, N., Margerin, L., Campillo, M., Van Tiggelen, B., Weaver, R., 2001. Observation of equipartition of seismic waves. Phys. Rev. Lett. 86, 3447.

Ibáñez, J.M., del Pezzo, E., Martini, M., Patané, D., de Miguel, F., Vidal, F., Morales, J., 1993. Estimates of coda-q using a non-linear regression. J. Phys. Earth 41, 203–219.

Johnston, D., Toksöz, M., 1981. Definitions and terminology: seismic wave attenuation, geophysics reprint series no. 2. Soc. Explor. Geophys Tulsa.

Li, X., Cormier, V.F., 2002. Frequency-dependent seismic attenuation in the inner core, 1. A viscoelastic interpretation. J. Geophys. Res. Solid Earth 107, ESE–13.

Margerin, L., 2017, May, May. Breakdown of equipartition in diffuse fields caused by energy leakage. The Eur. Phys. J. Spec. Top. 226, 1353–1370.

Margerin, L., Campillo, M., Tiggelen, B., 1998. Radiative transfer and diffusion of waves in a layered medium: new insight into coda q. Geophys. J. Int. 134, 596–612.

Margerin, L., Planès, T., Mayor, J., Calvet, M., 2015. Sensitivity kernels for coda-wave interferometry and scattering tomography: theory and numerical evaluation in two-dimensional anisotropically scattering media. Geophys. J. Int. 204, 650–666.

Margheriti, L., Amato, A., Braun, T., Cecere, G., D'Ambrosio, C., De Gori, P., Delladio, A., Gervasi, A., Govoni, A., Guerra, I., et al., 2013. Emergenza nell'area del pollino: le attività della rete sismica mobile. Rapporti Tecnici INGV.

Mayor, J., Margerin, L., Calvet, M., 2014. Sensitivity of coda waves to spatial variations of absorption and scattering: radiative transfer theory and 2-d examples. Geophys. J. Int. 197, 1117–1137.

Mayor, J., Calvet, M., Margerin, L., Vanderhaeghe, O., Traversa, P., 2016. Crustal structure of the Alps as seen by attenuation tomography. Earth Planet. Sci. Lett. 439, 71–80.

McNamara, D.E., Gee, L., Benz, H.M., Chapman, M., 2014. Frequency-dependent seismic attenuation in the eastern United States as observed from the 2011 central Virginia earthquake and aftershock sequence. Bull. Seismol. Soc. Am. 104, 55–72.

Menke, W., 2012. Geophysical Data Analysis: Discrete Inverse Theory (MATLAB Edition). Academic Press.

Napolitano, F., Gervasi, A., La Rocca, M., Guerra, I., Scarpa, R., 2018. Site effects in the Pollino region from the hvsr and polarization of seismic noise and earthquakes. Bulletin of the Seismological Society of America 108, 309–321.

Nishigami, K., 1991. A new inversion method of coda waveforms to determine spatial distribution of coda scatterers in the crust and uppermost mantle. Geophys. Res. Lett. 18, 2225–2228.

Obermann, A., Planès, T., Larose, E., Sens-Schönfelder, C., Campillo, M., 2013. Depth sensitivity of seismic coda waves to velocity perturbations in an elastic heterogeneous medium. Geophys. J. Int. 194, 372–382.

Ogiso, M., 2018. A method for mapping intrinsic attenuation factors and scattering coefficients of s waves in 3-d space and its application in southwestern Japan. Geophys. J. Int. 216, 948–957.

Paasschens, J., 1997. Solution of the time-dependent Boltzmann equation. Phys. Rev. E 56, 1135.

Pacheco, C., Snieder, R., 2005. Time-lapse travel time change of multiply scattered acoustic waves. J. Acoust. Soc. Am. 118, 1300–1310.

Parolai, S., 2014. Shear wave quality factor qs profiling using seismic noise data from microarrays. J. Seismol. 18, 695–704.

Picotti, S., Carcione, J.M., Rubino, J.G., Santos, J.E., Cavallini, F., 2010. A viscoelastic representation of wave attenuation in porous media. Comp. Geosci. 36, 44–53.

Prudencio, J., Ibá nez, J.M., García-Yeguas, A., Del Pezzo, E., Posadas, A.M., 2013. Spatial distribution of intrinsic and scattering seismic attenuation in active volcanic islands—II: Deception Island images. Geophysical Journal International 195, 1957–1969.

Prudencio, J., Aoki, Y., Takeo, M., Ibá nez, J.M., Del Pezzo, E., Song, W., 2017. Separation of scattering and intrinsic attenuation at Asama Volcano (Japan): evidence of high volcanic structural contrasts. J. Volcanol. Geoth. Res. 333, 96–103.

Przybilla, J., Wegler, U., Korn, M., 2009. Estimation of crustal scattering parameters with

elastic radiative transfer theory. Geophys. J. Int. 178, 1105–1111.

Rawlinson, N., Spakman, W., 2016. On the use of sensitivity tests in seismic tomography. Geophys. J. Int. 205, 1221–1243.

Rodríguez-Pradilla, G., 2015. Applications of shallow-seismic exploration methods for mechanical characterization of soil and rock bodies at engineering project sites in Colombia. Lead. Edge 34, 166–168.

Romanowicz, B., 1995. A global tomographic model of shear attenuation in the upper mantle. J. Geophys. Res. Solid Earth 100, 12375–12394.

Sanborn, C.J., Cormier, V.F., 2018. Modelling the blockage of lg waves from three-dimensional variations in crustal structure. Geophys. J. Int. 214, 1426–1440.

Sanborn, C.J., Cormier, V.F., Fitzpatrick, M., 2017. Combined effects of deterministic and statistical structure on high-frequency regional seismograms. Geophys. J. Int. 210, 1143–1159.

Sato, H., Fehler, M.C., Maeda, T., 2012. Seismic Wave Propagation and Scattering in the Heterogeneous Earth. vol. 496 Springer.

Souriau, A., Chaljub, E., Cornou, C., Margerin, L., Calvet, M., Maury, J., Wathelet, M., Grimaud, F., Ponsolles, C., Péquegnat, C., et al., 2011. Multimethod characterization of the French-Pyrenean valley of Bagnères-de-Bigorre for seismic-hazard evaluation: observations and models. Bull. Seismol. Soc. Am. 101, 1912–1937.

Takahashi, T., Sato, H., Nishimura, T., Obara, K., 2007. Strong inhomogeneity beneath quaternary volcanoes revealed from the peak delay analysis of s-wave seismograms of microearthquakes in northeastern Japan. Geophys. J. Int. 168, 90–99.

Takeuchi, N., 2016. Differential Monte Carlo method for computing seismogram envelopes and their partial derivatives. J. Geophys. Res. Solid Earth 121, 3428–3444.

Tisato, N., Quintal, B., Chapman, S., Podladchikov, Y., Burg, J.-P., 2015. Bubbles attenuate elastic waves at seismic frequencies: first experimental evidence. Geophys. Res. Lett. 42, 3880–3887.

Tramelli, A., Del Pezzo, E., Bianco, F., Boschi, E., 2006. 3D scattering image of the Campi Flegrei caldera (southern Italy): new hints on the position of the old caldera rim. Phys. Earth Planet. Inter. 155, 269–280.

Wang, W., Shearer, P., 2017. Using direct and coda wave envelopes to resolve the scattering and intrinsic attenuation structure of southern California. J. Geophys. Res. Solid Earth 122, 7236–7251.

Wang, W., Shearer, P., 2019. An improved method to determine coda-q, earthquake magnitude, and site amplification: theory and application to southern California. J. Geophys. Res. Solid Earth 124, 578–598.

Wegler, U., 2003. Analysis of multiple scattering at Vesuvius Volcano, Italy, using data of the Tomoves active seismic experiment. J. Volcanol. Geoth. Res. 128, 45–63.

Wegler, U., Lühr, B.G., 2001. Scattering behaviour at Merapi Volcano (Java) revealed from an active seismic experiment. Geophys. J. Int. 145, 579–592.

Xia, J., 2014. Estimation of near-surface shear-wave velocities and quality factors using multichannel analysis of surface-wave methods. Journal of Applied Geophysics 103, 140–151.